Received: 11 August 2022 | Revised: 14 October 2022 | Accepted: 15 October 2022

DOI: 10.1111/jace.18871

Journal of the American Ceramic Society

RESEARCH ARTICLE

On the anion and cation positions within and nearby $R(10\bar{1}2)$, $\Sigma(20\bar{2}4)$, and $\Pi(10\bar{1}4)$ planes of α-Al_2O_3 corundum structure

Vlado A. Lubarda[1] | **Marko V. Lubarda**[2]

[1]Department of NanoEngineering, University of California, San Diego, California, USA

[2]Department of Mechanical and Aerospace Engineering, University of California, San Diego, California, USA

Correspondence
Vlado A. Lubarda, Department of NanoEngineering, University of California, San Diego, CA, USA.
Email: vlubarda@ucsd.edu

Abstract

The positions of aluminum cations and oxygen anions within and nearby the $R(10\bar{1}2)$, $R'(30\bar{3}6)$, $\Sigma(20\bar{2}4)$, and $\Pi(10\bar{1}4)$ planes of α-Al_2O_3 corundum structure are determined and compared with the corresponding ion positions within and nearby their conjugate-adjacent planes $r(1\bar{1}02)$, $r'(3\bar{3}06)$, $\sigma(2\bar{2}04)$, and $\pi(1\bar{1}04)$ planes. The plane $R(10\bar{1}2)$ contains neither aluminum nor oxygen ions, while the planes $\pi(1\bar{1}04)$, $\Sigma(20\bar{2}4)$, and $\sigma(20\bar{2}4)$ contain only oxygen anions, whose planar densities are $\rho_\pi = 6/\text{nm}^2$ and $\rho_\Sigma = \rho_\sigma = 8.2/\text{nm}^2$. The planes $R'(30\bar{3}6)$, $r'(3\bar{3}06)$, and $r(1\bar{1}02)$ contain only aluminum cations with planar densities $\rho_{R'} = 8.2/\text{nm}^2$ and $\rho_\text{r} = \rho_{\text{r}'} = 5.47/\text{nm}^2$. The $\Pi(10\bar{1}4)$ plane contains both aluminum and oxygen ions, whose planar densities are $\rho_\Pi^{\text{Al}} = 4/\text{nm}^2$ and $\rho_\Pi^{\text{O}} = 6/\text{nm}^2$. The nearest ions to the $R(10\bar{1}2)$, $r(1\bar{1}02)$, $R'(30\bar{3}6)$, and $r'(3\bar{3}06)$ planes are at a normal distance of 0.58 Å from these planes, which is one-half of the normal distance between the adjacent R and R', or r and r' planes. The ions nearest to the $\Sigma(20\bar{2}4)$ and $\sigma(2\bar{2}04)$ planes are also at a normal distance of 0.58 Å from these planes. The nearest ions to the $\Pi(10\bar{1}4)$ and $\pi(1\bar{1}04)$ planes are 0.85 Å from these planes, which is one-half the interplanar spacing between the adjacent Π or π planes. The obtained results are of interest for the evaluation of ionic bonding and surface energies, epitaxial film growth over differently oriented sapphire substrates, and for the analysis of plastic deformation and cleavage fracture of sapphire crystals under different loading and temperature conditions.

KEYWORDS
alumina, corundum, dislocations, layered crystal structures, plasticity

1 | INTRODUCTION

A thermodynamically stable form of aluminum oxide Al_2O_3 at standard temperature and pressure, known as α-Al_2O_3 or sapphire, has the corundum structure in which the oxygen anions are closely packed in planes stacked in the hexagonal closed-packed (HCP) sequence A–B–A–B–..., while the aluminum cations occupy two-thirds of the octahedral interstitial sites in between the oxygen planes, forming the sequence a–b–c–a–b–c–... of cation layers horizontally shifted relative to each other.[1,2] The overall structure is a repetition of the stacking sequence A–a–B–b–A–c–B–a–A–b–B–c–A, as shown in Figure 1; metastable polymorphs of Al_2O_3 are reviewed in reference.[3] The basal planes of closely packed oxide anions are flat. Since aluminum cations occupy only two-thirds of available

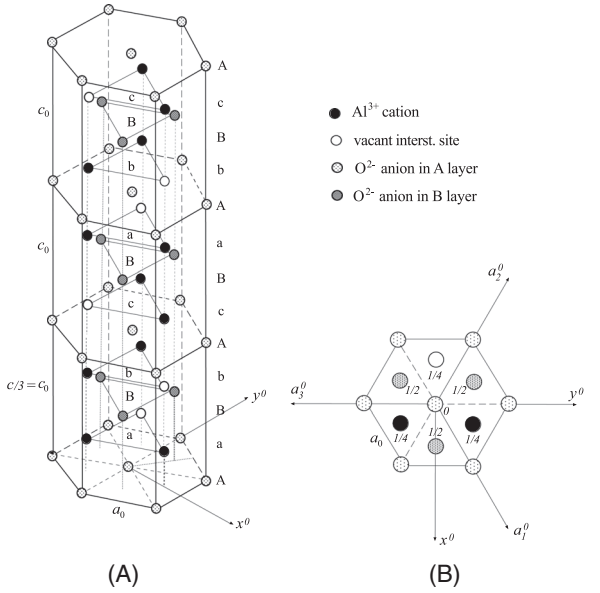

FIGURE 1 (A) A stacking sequence *A–a–B–b–A–c–B–a–A–b–B–c–A* of the α-Al_2O_3 corundum structure. The oxygen anions O^{2-} are closely packed in planes which are stacked in an HCP sequence *A–B–A–B–A–B–A* of height $c = 3c_0$. The aluminum cations Al^{3+} occupy two-thirds of octahedral interstitial sites in between the oxygen planes *A* and *B*, forming a sequence *a–b–c–a–b–c*. (b) The oxygen anions from the *B*-layer are by $c_0/2$ above (and below) the oxygen anions from the basal *A*-layer. The aluminum cations are in between *A* and *B* layers, at the distance $c_0/4$ from them. The hexagonal axes within the oxygen basal layer *A* are (a_1^0, a_2^0, a_3^0).

octahedral interstitial sites, they are slightly non-coplanar in their basal planes, because of the corresponding adjustments of cation positions caused by interionic interactions. This slight distortion of the corundum structure is usually ignored in analytical studies. Thus, by denoting the height of the structural sequence *A–a–B–b–A–c–B–a–A–b–B–c–A* by c, the normal distance between two adjacent oxygen and aluminum layers (e.g., *A* and *a*) is $c/12$, while the distance between two adjacent oxygen layers (*A* and *B*), or two adjacent aluminum layers (*a* and *b*, *b* and *c*, or *c* and *a*) is $c/6$. The actual vertical distances between aluminum cations, inferred from x-ray diffraction measurements, alternate between about $0.204c$ and $0.296c$, depending on whether there is a vacant interstitial site in between the cations or not. For example, the aluminum cations above the vacant interstitial site at $z = 0$ are located at $z/c = (0.148, 0.352, 0.5, 0.648, 0.852)$.[4–6] Eighteen (18) oxygen anions and 12 aluminum cations belong to the shown hexagonal prism of height $c = 3c_0$ and edge a_0, where a_0 is the distance between two neighboring oxygen anions, or two neighboring aluminum cations within their basal planes.

The aluminum sublattice, showing only the aluminum cations and the vacant interstitial sites from the sequence *a–b–c–a*, is shown in Figure 2A. The height of the shown prism is $c/2$. The embedded oxygen layers *B–A–B* from the morphological sequence *a–B–b–A–c–B–a* are not shown in Figure 2A. The smallest hexagonal prism (unit cell) which fully describes the repetitive pattern of cation positions has the hexagonal base (dotted line in Figure 2A) of side a, representing the distance between two neighboring vacant interstitial sites (e.g., a_1 and a_2) within the layer a. The use of such hexagonal mesh was proposed by Kronberg[2] and was subsequently adopted in most other related work.[4,7,8] The early study of the corundum structure of sapphire was reported by Pauling and Hendricks.[1] The smallest structural hexagonal prism (unit cell) which fully describes the positions of aluminum cations and embeds the entire oxygen layer sequence *B–A–B–A–B–A*, is twice the height of the morphological hexagonal unit cell shown in Figure 2. The positions of aluminum cations and vacant interstitial sites within three hexagons from the consecutive layers *a*, *b*, and *c* are shown in Figure 3. The cation patterns *a*, *b*, and *c* can also be recognized within a single basal plane of cations (Figure 4), since they are horizontally shifted relative to each other by the distance (a_0) between two nearest cations in that plane.

The space group symmetry of α-Al_2O_3 is $R\bar{3}c$ (three-fold rotation with inversion), and its crystal class is trigonal[9–12] (space group number 167). The experimentally determined lattice parameters of sapphire (a and c) at room temperature are approximately $a = 4.758$ Å and $c = 12.992$ Å, as reported in references[4,5,7,13,14]; the measured values of a and c in the temperature range of 10-1166 K, with a fit by the Debye model, are reported in reference.[15] Thus, the distance between the oxygen layers *A* or *B* is $c/3 = 4.33$ Å, which is about 1.57 times the ionic diameter of O^{2-} ($2R_{O^{2-}} = 2 \times 1.38$ Å $= 2.76$ Å). As discussed by Kronberg,[2] the factor 1.57 is smaller than the factor $\sqrt{8/3} = 1.63$ corresponding to perfect HCP packing of spheres, as a result of the attractive forces between alternating layers of aluminum cations and oxygen anions. The radius of aluminum cations ($R_{Al^{3+}} = 0.535$ Å) is slightly smaller than the radius of the interstitial site in the oxygen sublattice, which is $(\sqrt{2} - 1)R_{O^{2-}} \approx 0.57$ Å. The distance between oxygen anions in the direction of the closest packing is $a_0 = a/\sqrt{3}$, which follows from geometry because $h = a\sqrt{3}/2 = 3a_0/2$. The orientation of the hexagonal mesh formed by oxygen anions differs by a 30° rotation about the mesh normal, and its center is shifted by $a/3$ in the basal plane (Figure 5). The basal *A*-layer of oxygen anions is by $c/12$ below the basal *a*-layer of aluminum cations. It is also noted that $c/a = 2.731$ and $c_0/a_0 = 1.576$, while in an ideal HCP structure these ratios would be $\sqrt{8} = 2.828$ and $\sqrt{8/3} = 1.633$.

The angle between the rhomboidal axes a_1^r and a_2^r, a_2^r and a_3^r, and a_3^r and a_1^r is $\alpha = 55.28°$. The length

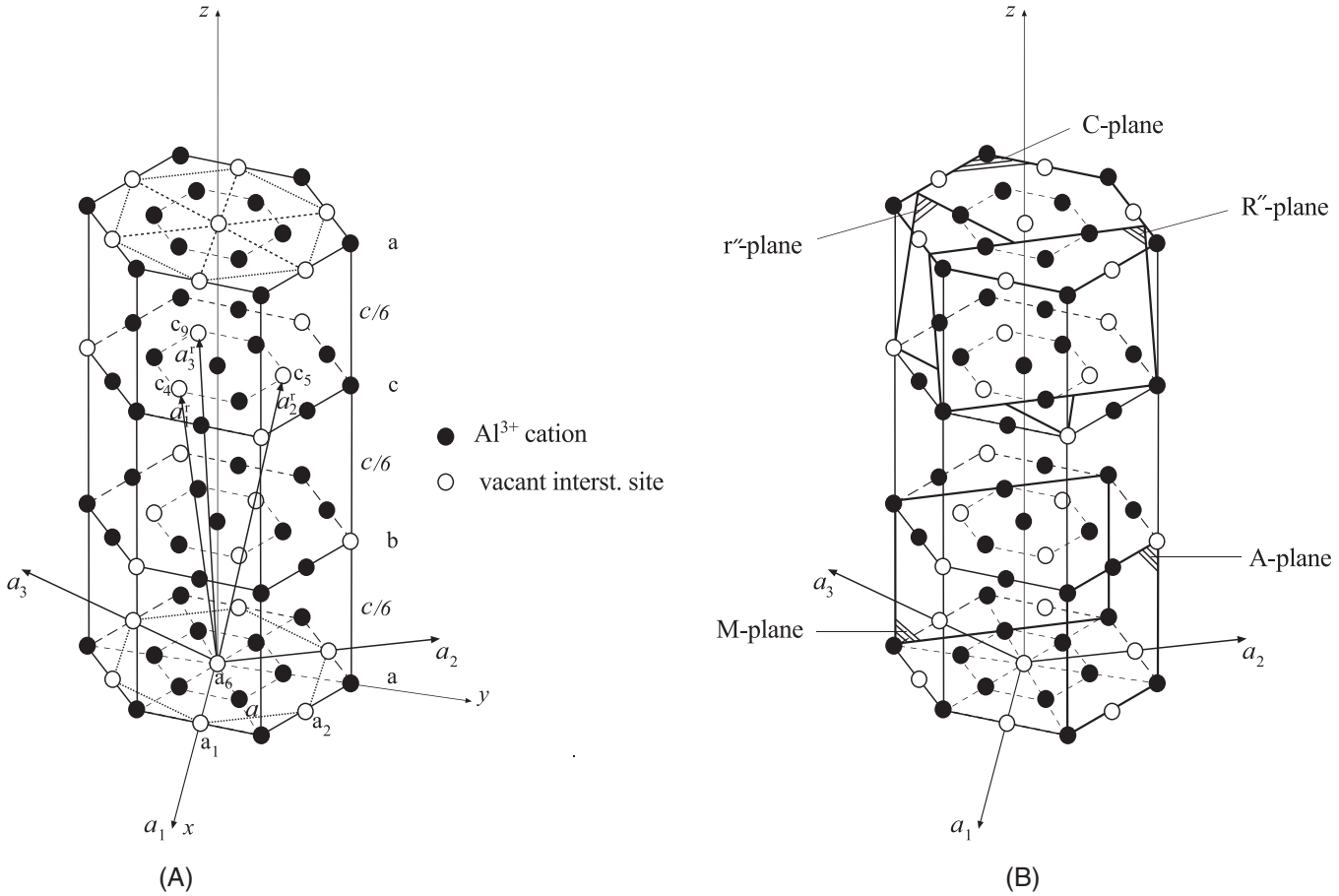

FIGURE 2 (A) The hexagonal prism of height $c/2 = 6.496$ Å showing the positions of aluminum cations and vacant interstitial sites in four sequential cation layers a–b–c–a. The distance between two nearby vacant interstitial sites within the basal a-layer, such as a_1 and a_2, is $a = 4.758$ Å. The hexagonal axes with the origin at the center of the vacant interstitial site in the bottom a-layer are (a_1, a_2, a_3). The rhomboidal axes of the structural cell of height c are (a_1^r, a_2^r, a_3^r), which pass through vacant interstitial sites c_4, c_5, and c_9. (B) The segments of prismatic $A(11\bar{2}0)$ and $M(\bar{1}010)$ planes, rhombohedral $R''(30\bar{3}6)$ and $r''(3\bar{3}06)$ planes, and basal $C(0001)$ plane.

$\overline{a_6c_4} = \overline{a_6c_5} = \overline{a_6c_9} = [(2h/3)^2 + (c/3)^2]^{1/2} = 5.128$ Å is the length of the edge of the smallest structural rhombohedral cell (of height c) which properly describes the positions of four consecutive aluminum cations along the vertical z-direction (in a non-distorted structure at $z/c = 1/6, 1/3, 2/3, 5/6$).

Our objective in this paper is to determine the positions of aluminum and oxygen ions which are located within and in the closest proximity to distinct crystallographic planes of sapphire, which include the $R(10\bar{1}2)$, $R'(30\bar{3}6)$, $\Sigma(20\bar{2}4)$, and $\Pi(10\bar{1}4)$ planes, and their adjacent $r(1\bar{1}02)$, $r'(3\bar{3}06)$, $\sigma(2\bar{2}04)$, and $\pi(1\bar{1}04)$ planes. In order to determine the repetitive patterns of aluminum and oxygen ions, and their corresponding planar and line densities, the ionic positions within the original unit cell and within the neighboring unit cells, have been considered. This may be of interest for the evaluation of ionic bonding strengths,[16,17] surface energies,[18,19] epitaxial film growth over differently oriented sapphire substrates,[20–22] self-healing of surface cracks at elevated temperature,[23,24] and for the analysis of inelastic deformation and cleavage fracture of sapphire crystals.[25–31] Mechanical, thermal, electrical, and optical properties of sapphire substrates and wafers, which guide their use, are directly related to the orientation of the free surface relative to the bulk crystalline structure. The surface ions adjust their positions relative to the interior of the crystal to minimize the free energy and create a thermodynamically stable surface. The ionic configurations in the vicinity of this surface define the surface energy, and affect diffusion paths and surface transport of dispersed particles used in doping (e.g., strengthening and toughening by carbon or titanium[32]), or as catalysts to enhance thin film or other nanostructural growth. For example, single-walled carbon nanotubes with best horizontal alignment are grown on the A- and R-plane oriented sapphire substrates.[33] The surface energies of different crystallographic planes are directly related to the fracture toughness (critical stress intensity factor) with respect to these planes. Fracture can occur over a weak cleavage plane, with a low surface energy, even if

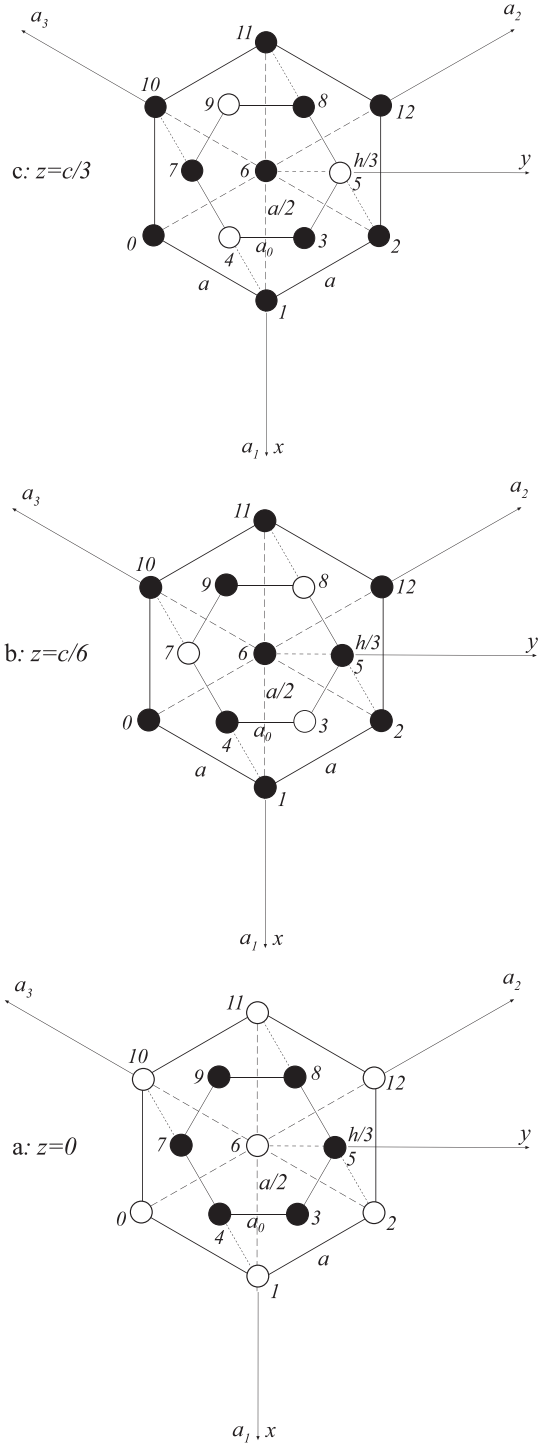

FIGURE 3 The positions of aluminum cations and vacant interstitial sites in three sequential cation layers a, b, and c. The distance between two nearby vacant interstitial sites within each basal plane is a. The distance between two neighboring aluminum cations is $a_0 = 2h/3 = a/\sqrt{3}$, where $h = \sqrt{3}a/2$. The (x, y) coordinates of 13 shown points used in the subsequent analysis of ionic configurations within and around considered crystallographic planes are: $0(a/2, -h)$, $1(a, 0)$, $2(a/2, h)$, $3(a/2, h/3)$, $4(a/2, -h/3)$, $5(0, 2h/3)$, $6(0,0)$, $7(0, -2h/3)$, $8(-a/2, h/3)$, $9(-a/2, -h/3)$, $10(-a/2, -h)$, $11(-a, 0)$, and $12(-a/2, h)$. The z-coordinates of the layers a, b, and c are $z = 0$, $c/6$, and $c/3$.

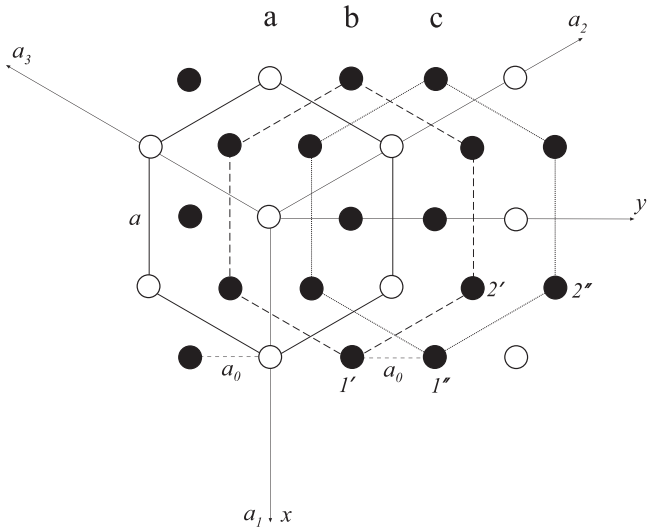

FIGURE 4 Three hexagons with cation patterns a, b, and c which are in Figure 3 located above each other, can also be identified within a single cation plane; they are horizontally shifted relative to each by $a_0 = a/\sqrt{3}$, the distance between two nearest cations in their basal plane. The normal distance between two parallel planes with unit normal vector $\mathbf{n} = \{n_x, n_y, n_z\}$, one passing through cations 1′ and 2′, and the other through cations 1″ and 2″, is $d = \mathbf{n} \cdot a_0\mathbf{e}_y = n_y a_0$, where $\mathbf{e}_y$ is the unit vector along the y-direction.

it is not under the highest tensile stress. The fracture surface energy on the prismatic $\{10\bar{1}0\}$ and the rhombohedral $\{\bar{1}012\}$ planes was measured to be about 7.3 and 6.0 J/m^2, respectively. Various factors related to the ionic structure affect the fracture toughness of sapphire crystals. In experiments using the double-cantilever-cleavage technique with a differently oriented crack plane relative to the crystallographic axes of the crystal, the lack of fracture along the basal (0001) plane was attributed to the lack of the electrostatic charge neutrality of this plane.[34] The energy calculations using the self-consistent local-density variational method showed that the surface with the lowest cleavage energy is terminated with an aluminum layer for the (0001) surface, while it is terminated with an oxygen layer for the $(1\bar{1}02)$ surface.[16] Furthermore, the ionic configuration determines the lattice friction stress, which depends on the dislocation Burgers vector and the crystallographic planar spacing. Because during slip the shearing oxygen layer moves over the underlying oxygen layer, as well as the intervening interstitial cations, the length of the dislocation Burgers vector for the basal slip (0001) $<11\bar{2}0>$ is equal to a, which is the smallest structural translation which restores the structure. At the temperature above 900 °C, single crystals of sapphire undergo plastic deformation by slip over basal (0001) planes in $<11\bar{2}0>$ directions; at even higher temperatures plasticity may take place by slip on prismatic A-planes $\{1\bar{2}10\}$ in the $<10\bar{1}0>$

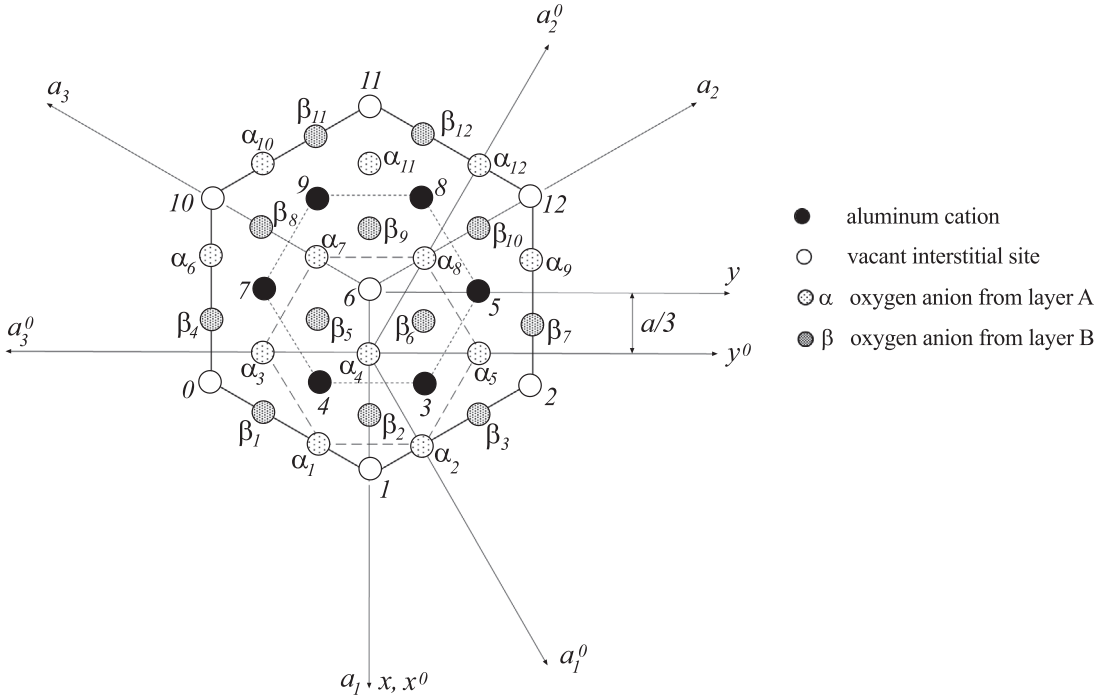

FIGURE 5 Projections of the centers of aluminum cations, oxygen anions, and vacant interstitial sites onto the basal planes of cations or anions. The coordinate origin α_4 for the axes (x^0, y^0) and (a_1^0, a_2^0, a_3^0) within the basal A-layer of oxygen anions is by $c/12$ below the basal a-layer of aluminum cations ($z = 0$); thus $z_0 = z + c/12$. The hexagonal axes (a_1^0, a_2^0, a_3^0) are by 30° counterclockwise from the hexagonal axes (a_1, a_2, a_3) within the basal a-layer of aluminum cations. The (x, y) coordinates of aluminum cations and vacant interstitial sites are listed in the caption of Figure 3. The (x^0, y^0) coordinates of the α-oxygen anions are $\alpha_1(h_0, -a_0/2)$, $\alpha_2(h_0, a_0/2)$, $\alpha_3(0, -a_0)$, $\alpha_4(0, 0)$, $\alpha_5(0, a_0)$, $\alpha_6(-h_0, -3a_0/2)$, $\alpha_7(-h_0, -a_0/2)$, $\alpha_8(-h_0, a_0/2)$, $\alpha_9(-h_0, 3a_0/2)$, $\alpha_{10}(-2h_0, -a_0)$, $\alpha_{11}(-2h_0, 0)$, and $\alpha_{12}(-2h_0, a_0)$. The (x^0, y^0) coordinates of the oxygen anions β_1 and β_4 are $\beta_1(2h_0/3, -a_0)$ and $\beta_4(-h_0/3, -3a_0/2)$, while the coordinates of β_2, β_3, β_5, β_6, β_7, β_8, β_9, β_{10}, β_{11}, β_{12} are obtained from the coordinates α_1, α_2, α_3, α_4, α_5, α_6, α_7, α_8, α_{10}, α_{11} by using the transformation $x_\beta^0 = x_\alpha^0 - h_0/3$ and $y_\beta^0 = y_\alpha^0 + a_0/2$. The (x, y) and (x^0, y^0) coordinates are related by $x = x^0 + 2h_0/3$ and $y = y^0$. The length of the solid-line hexagon sides is $a = \sqrt{3}a_0 = 2h_0$, where a_0 is the length of the dashed- and dotted-line hexagon sides. The periodicity of the overall structure in a_1, a_2, and a_3 directions is equal to a.

or $<10\bar{1}1>$ directions, and on the pyramidal slip systems $\{1\bar{1}02\}<01\bar{1}1>$ and $\{10\bar{1}1\}<01\bar{1}1>$ within the sapphire R- and S-planes.[26,35,36] Dissociation of total dislocations into their partials during crystallographic slip over the basal plane is accompanied by co-operative movements of anions and cations to reduce the total dislocation energy. This gives rise to plastic deformation by gliding of four partial dislocations separated by stacking faults.[2,36–41] A recent survey of dislocation mechanics in ceramics is given in reference.[42] Molecular dynamics simulations of edge dislocations within basal and pyramidal planes of sapphire have been conducted by many investigators, as reported, for example, in references.[43,44]

2 | RHOMBOHEDRAL R(10$\bar{1}$2) AND R′(30$\bar{3}$6) PLANES

Sapphire is a ceramic material which is frequently used in the microelectronic industry as a substrate material for film growth. Although the (0001) plane sapphire substrates are most commonly used, for some applications the rhombohedral sapphire substrates are chosen because of their potential for improved luminous efficiency of light-emitting diode (LED) devices, improved fabrication processes, and resistance to subsurface damage.[21,45–47] Figure 6A shows three parallel crystallographic planes of the structural hexagonal prism of height $c = 12.992$ Å. The $R(10\bar{1}2)$ plane passes through the interstitial sites with (x, y, z) coordinates $a_1(a, 0, 0)$, $a_2(a/2, h, 0)$, $b_3(a/2, h/3, c/6)$, $c_4(a/2, -h/3, c/3)$, $c_5(0, 2h/3, c/3)$, and $\hat{a}_6(0, 0, c/2)$, having the equation $x/a + y/(2h) + 2z/c = 1$. The normal distance between two adjacent $R(10\bar{1}2)$ planes is $d_R = 3.48$ Å. The plane $R(10\bar{1}2)$ is parallel to the rhomboidal axis a_3^r, and intersects the axes a_1^r and a_2^r at points c_4 and c_5, which are at the distance $b = 5.128$ Å from the coordinate origin at point a_6; thus its Miller indices with respect to the rhombohedral axes are $R(110)_r$.

The plane $R'(30\bar{3}6)$, parallel to the $R(10\bar{1}2)$ plane and at a normal distance of 2.32 Å from that plane, passes through the centers of aluminum cations a_4, a_5, and $\hat{a}_9$, thus having the equation $3x/a + 3y/(2h) + 6z/c = 1$. The

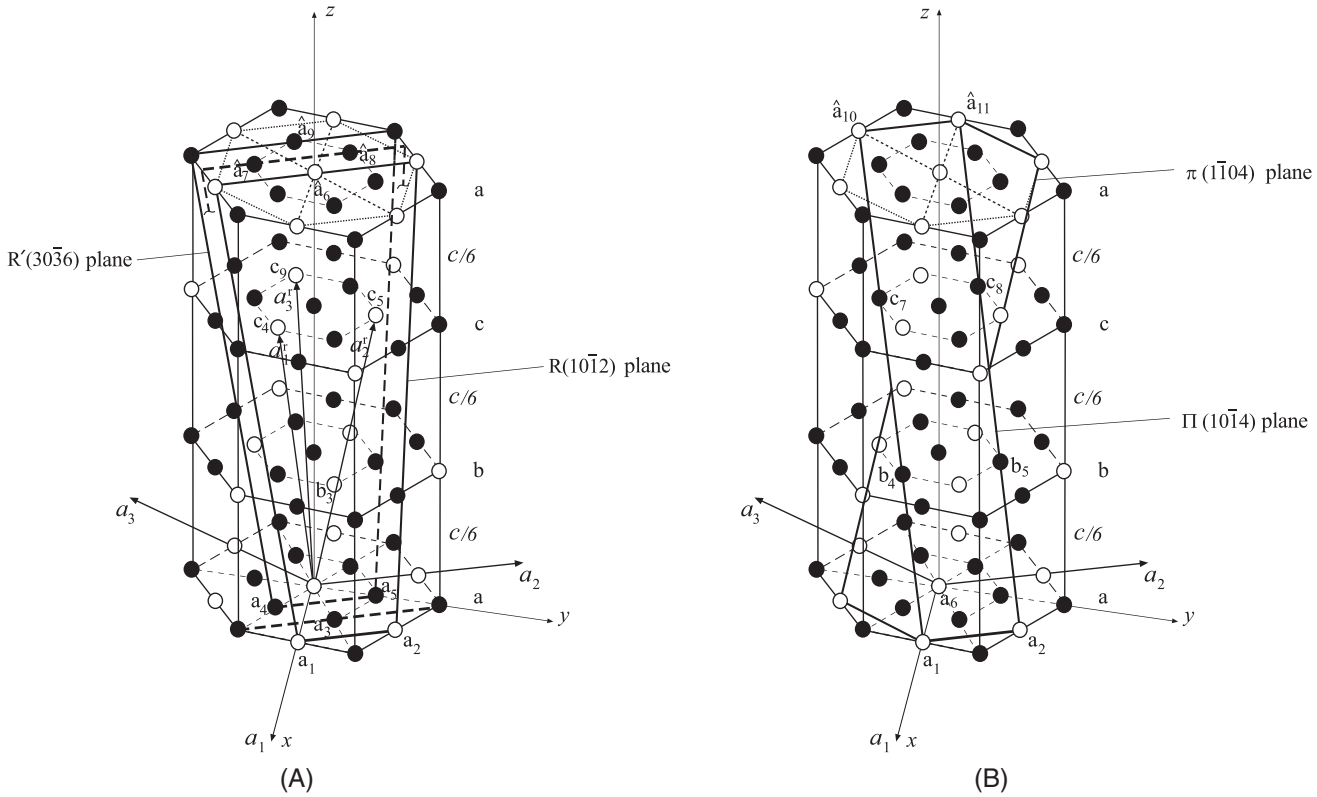

FIGURE 6 (A) The R(10$\bar{1}$2) plane passes through vacant interstitial sites a_1, a_2, b_3, c_4, c_5, and $\hat{a}_6$. The plane $R'(30\bar{3}6)$ is parallel to $R(10\bar{1}2)$ plane, and passes through aluminum cations at a_4, a_5, and $\hat{a}_9$. Another crystallographically equivalent plane $R''(30\bar{3}6)$ passes through cations at a_3, $\hat{a}_7$, and $\hat{a}_8$ (shown truncated and in the dashed line). (b) The $\Pi(10\bar{1}4)$ plane passes through vacant interstitial sites at a_1, a_2, $\hat{a}_{10}$, $\hat{a}_{11}$, and aluminum cations at b_4, b_5, c_7, c_8. The attached hat for points such as $\hat{a}_6$ and $\hat{a}_{10}$ indicates that a point is from the upper a-layer, at $z = c/2$. Also shown is the adjacent $\pi(1\bar{1}04)$ plane.

third plane, shown truncated in Figure 6A and having the equation $3x/2a + 3y/(4h) + 3z/c = 1$, is in the middle in between the $R(10\bar{1}2)$ and $R'(30\bar{3}6)$ planes (being at the normal distance $d_{R'} = d_R/3 = 1.16$ Å from both), and is crystallographically equivalent to the $R'(30\bar{3}6)$ plane (R'' intersects the z-axis at $z = c/3$, while R' intersects the z-axis at $z = c/6$). The unit vector orthogonal to all three planes is $\mathbf{n}_R = \{0.7313, 0.4222, 0.5356\}$, which makes an angle of 57.61° with the z-axis.

Note: If the coordinate origin of the (a_1, a_2, a_3) hexagonal axes was at the center of the hexagon in the c-layer (at $c/6$ below the a-layer), the indices of the $R'(30\bar{3}6)_a$ plane would be $R'(10\bar{1}2)_c$. Similarly, if the coordinate origin was at the center of the hexagon in the b-layer (at $c/3$ below the a-layer), the indices of the $R''(30\bar{3}6)_a$ plane would be $R''(10\bar{1}2)_b$. The subscripts a,b, and c are added to indicate the cation layer in which the coordinate origin is placed. Also, the more common indices for the R-plane $(1\bar{1}02)$ used in the literature correspond the choice of hexagonal axes obtained by 120° clockwise rotation from the axes (a_1, a_2, a_3) shown in Figure 2.

Figure 7A shows the locations of vacant interstitial sites within the segment of the $R(10\bar{1}2)$ plane. The distances $\overline{a_1a_2} = a = 4.758$ Å, $\overline{a_1c_4} = b = 5.128$ Å, and $\overline{a_1b_3} = 3.498$ Å. There are no aluminum cations within the $R(10\bar{1}2)$ plane, so their planar density within this plane is equal to zero. Figures 7B,C show the locations of the centers of aluminum cations within the segment of the parallel planes R' and R'', having the same Miller–Bravais indices $(30\bar{3}6)$. The corresponding planar density of aluminum cations is $2/(ab) = 8.2/\text{nm}^2$. The close-packed direction of aluminum cations within the $R'(30\bar{3}6)$ plane is the direction $[\bar{2}201]$ (from a_3 to b_5), with the cation separation distance equal to $(1/2)\sqrt{a^2 + b^2} = 3.498$ Å. Two other crystallographically equivalent planes, $(\bar{3}306)$ and $(0\bar{3}36)$, also have the cation density $2/(ab) = 8.2/\text{nm}^2$. The dislocation Burgers vectors for the observed slip over the R'-plane are of magnitude a along $[\bar{1}2\bar{1}0]$, and b along $[\bar{1}101]$ direction (Figure 7).[26]

For the sake of comparison, the planar density of cations in the basal $C(0001)$ plane is $2/(ah) = 10.2/\text{nm}^2$, while the planar density in the prismatic $A(11\bar{2}0)$ and $M(10\bar{1}0)$ planes are $6/(hc) = 11.21/\text{nm}^2$ and $4/(ac) = 6.47/\text{nm}^2$, respectively ($C$, A, and M being the mineralogical symbols for these planes[48]). Segments of C, A, and M planes are sketched in Figure 2B. Sapphire wafers of other

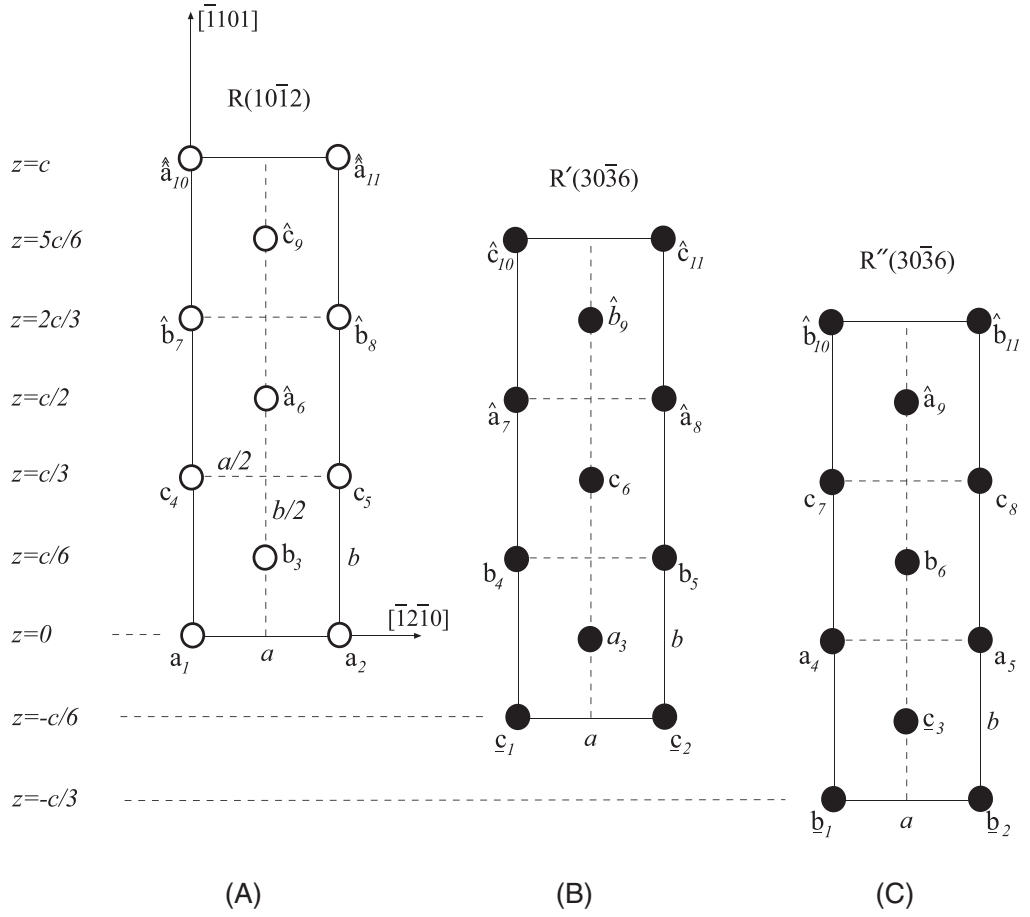

FIGURE 7 (A) The locations of vacant interstitial sites (open circles) within the segment of the $R(10\bar{1}2)$ plane of the structural hexagonal prism of height $c = 12.992$ Å. There are no aluminum cations within $R(10\bar{1}2)$ plane. (B,C) The locations of the centers of aluminum cations (black circles) within the segment of the crystallographically equivalent planes R' and R″, having the same Miller–Bravais indices $(30\bar{3}6)$. The attached hat for points such as $\hat{a}_6$ indicates that a point is from the a-layer is at $z = c/2$, while $\hat{a}_{10}$ indicates that a point is at $z = c$. Similarly, $\underline{c}_1$ indicates that a point is at $z = -c/6$, rather than $z = c/3$.

orientations have also been studied and used, including N-plane $(11\bar{2}3)$ and V-plane $(22\bar{4}3)$ sapphire wafers.[49–51] Differently oriented sapphire wafers have different physical properties which enable their different technological applications.[21,32,45,46,52] In silicon on sapphire (SOS) wafer applications,[53,54] the lattice mismatch is $a^{Si}/a = 1.14$ and $a^{Si}/b = 1.06$, because $a^{Si} = 5.431$ Å. Selected physical properties of sapphire crystals and their uses have been discussed, inter alia, in references.[8,55–58]

2.1 | Rhombohedral r$(1\bar{1}02)$ plane

Because the corundum structure has the three-fold symmetry with respect to 120° rotation around the c-axis, the plane r$(1\bar{1}02)$, having the equation $x/a - y/(2h) + 2z/c = 1$ and cation density $1/(ab) = 4.1/\text{nm}^2$, is crystallographically different from the plane $R(10\bar{1}2)$. The cation density for the two parallel planes $(3\bar{3}06)$, with equations $3x/a - 3y/(2h) + 6z/c = 1$ and $3x/2a - 3y/(4h) + 3z/c = 1$, is $4/(3ab) = 5.47/\text{nm}^2$ (Figure 8). The centers of the oxygen anions nearest to the $r(1\bar{1}02)$ plane are at a normal distance of 0.58 Å from the r-plane and are shown in Figure 9C.

2.2 | Calculation of interplanar distances

The interplanar distances for sapphire crystallographic planes can be calculated in various ways. Using the rhombohedral lattice parameters b and α, the normal distance between two adjacent $R(110)_r$ planes is [11, 59]

$$d_R = \frac{b}{N},$$

$$N = \left[\frac{(H^2 + K^2 + L^2)\sin^2\alpha + 2(HK + KL + LH)(\cos^2\alpha - \cos\alpha)}{1 - 3\cos^2\alpha + 2\cos^3\alpha}\right]^{1/2}, \tag{2.1}$$

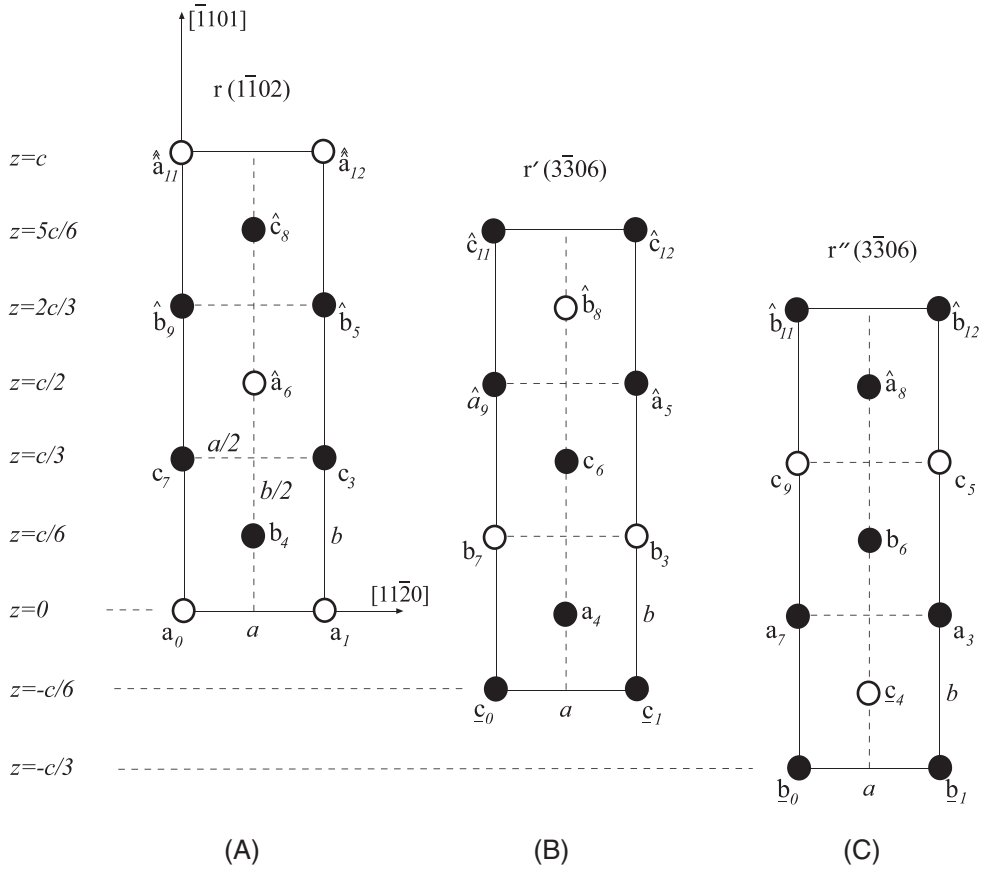

FIGURE 8 The locations of aluminum cations (black circles) and vacant interstitial sites (open circles) within the segment of the plane $r(1\bar{1}02)$, and two crystallographically equivalent planes r' and r'', having the same Miller–Bravais indices $r(3\bar{3}06)$. The normal distance between r and r', or r' and r'' planes is $d_r/3 = 1.16$ Å, where the distance between two adjacent r(1$\bar{1}$02) planes is $d_r = 3.48$ Å.

where $H = K = 1$ and $L = 0$ are the Miller indices of the R plane with respect to the rhombohedral axes (a_1^r, a_2^r, a_3^r). Thus,

$$d_R = \frac{b}{N} = 3.48\,\forall\,, \quad N = \left(\frac{2}{\cos\alpha - \cos 2\alpha}\right)^{1/2} = 1.4738\,, \tag{2.2}$$

because $\alpha = 55.28°$ and $b = 5.128$ Å.

If the hexagonal axes (a_1, a_2, a_3) and the corresponding hexagonal lattice parameters a and c are used instead, the interplanar distance between two adjacent $R(10\bar{1}2)_h$ planes can be determined from [11,60]

$$d_R = \frac{a}{N_0} = 3.48\,\forall,$$

$$N_0 = \left[\frac{4}{3}\left(h^2 + k^2 + hk\right) + l^2\left(\frac{a}{c}\right)^2\right]^{1/2} = \frac{2}{\sqrt{3}}\sqrt{1 + 3(a/c)^2} = 1.3674, \tag{2.3}$$

because $h = 1$, $k = 0$, $l = 2$, $a = 4.758$ Å, and $c = 12.992$ Å $(a/c = 0.3662)$.

The interplanar distance can also be calculated from the geometrical expression for the normal distance of the point $(x_0, y_0, z_0) = (0, 0, 0)$ from the plane $mx + ny + pz + q = 0$, which is

$$d_R = \frac{|mx_0 + ny_0 + pz_0 + q|}{(m^2 + n^2 + p^2)^{1/2}} = \frac{|q|}{(m^2 + n^2 + p^2)^{1/2}}. \tag{2.4}$$

Since for the $R(10\bar{1}2)$ plane, $m = 1/a$, $n = 1/(2h)$, $p = 2/c$, and $q = -1$, Equation (2.4) gives

$$d_R = \frac{ch}{\sqrt{c^2 + 4h^2}} = 3.48\,\forall\,. \tag{2.5}$$

Finally, referring to Figure 4, the interplanar distance between two parallel R-planes passing through vacancy interstitial sites is $d_R = 3a_0 n_y = 3.48$ Å, where $a_0 = a/\sqrt{3} = 2.747$ Å is the distance between the nearest cations in the basal a-layer, and $n_y = 0.4222$ is the y-component of the unit vector $\mathbf{n}_R = \{0.7313, 0.4222, 0.5356\}$ orthogonal to the R-plane.

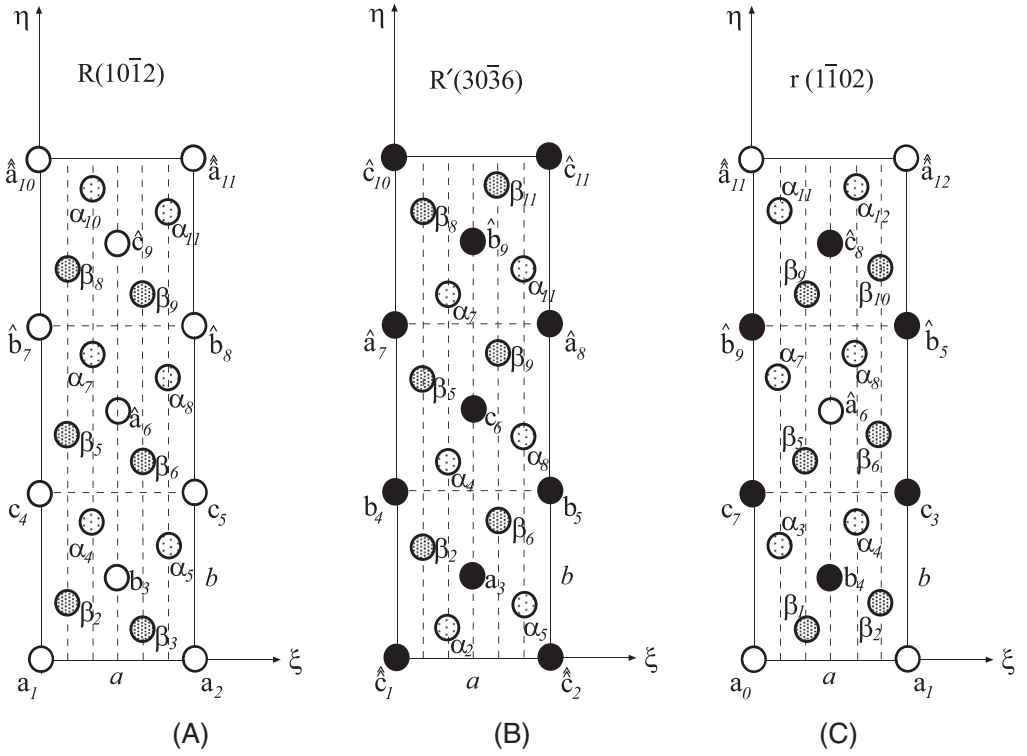

FIGURE 9 (A) The oxygen anions from A-layers (dotted α circles) and B-layers (shaded β circles) nearest to the $R(10\bar{1}2)$ plane are at a normal distance of 0.58 Å from that plane. The open circles are the vacant interstitial sites within the R-plane. The attached hat over a, b, and c indicates a cation layer at different heights z. Shown are the (ξ, η) coordinates of the projected centers of oxygen anions. The oxygen anions α_5, α_8, α_{11}, β_3, β_6, and β_9 are above, while α_4, α_7, α_{10}, β_2, β_5, and β_8 are below the R-plane. (B) Same as in part (A), but for the $R'(30\bar{3}6)$ plane. The oxygen anions α_2, α_4, α_7, β_2, β_5, and β_8 are below, while α_5, α_8, α_{11}, β_3, β_6, β_9, and β_{11} are above the $R'(30\bar{3}6)$ plane. Black circles are the aluminum cations within the R'-plane. (C) The oxygen anions nearest to the $r(1\bar{1}02)$ plane are at a normal distance of 0.58 Å from that plane. The oxygen anions α_3, α_7, and α_{11}, β_1, β_5, and β_9 are above, while α_4, α_8, α_{12}, β_2, β_6, and β_{10} are below the r-plane.

2.3 | Oxygen anions nearby the *R*-plane

Figure 9A shows the oxygen anions from the A-layers (dotted α circles) and B-layers (shaded β circles) nearest to the $R(10\bar{1}2)$ plane. They are at the normal distance $d = d_{R'}/2 = 0.58$ Å from that plane, where $d_{R'} = 1.16$ Å is the interplanar distance between adjacent R' and R'' planes, or the normal distance between the R plane and a nearby R' or R'' plane. The open circles are the vacant interstitial sites within the R-plane. The nearest oxygen anions from the A-layers are within the plane $2x/a + 3z/c = 17/12$, and their centers are at points $\alpha_2(5a/6, h/3, -c/12)$, $\alpha_4(a/3, 0, c/4)$, $\alpha_5(a/3, 2h/3, c/4)$, $\alpha_7(-a/6, -h/3, 7c/12)$, $\alpha_8(-a/6, h/3, 7c/12)$, $\alpha_{10}(-2a/3, -2h/3, 11c/12)$, and $\alpha_{11}(-2a/3, 0, 11c/12)$. The nearest oxygen anions from the B-layers are within the plane $2x/a + 3z/c = 19/12$ and their centers are at points $\beta_2(2a/3, 0, c/12)$, $\beta_3(2a/3, 2h/3, c/12)$, $\beta_5(a/6, -h/3, 5c/12)$, $\beta_6(a/6, h/3, 5c/12)$, $\beta_8(-a/3, -2h/3, 3c/4)$, and $\beta_{11}(-5a/6, -h/3, 13c/12)$. The (ξ, η) coordinates of the projected centers of oxygen anions α_4 and α_5 onto the R-plane are $\alpha_4(a/3, 0.8217b)$ and $\alpha_5(5a/6, 0.6783b)$, and likewise for α_7, α_8, and α_{10}, α_{11}, the latter being shifted in the η direction by b and $2b$, where $b = 5.128$ Å. The oxygen anion α_5, α_8, and α_{11} are above, while α_4, α_7, and α_{10} are below the R-plane. The (ξ, η) coordinates of the projected centers of oxygen anions β_2 and β_3 are $\beta_2(a/6, 0.3217b)$ and $\beta_3(2a/3, 0.1783b)$, and likewise for β_5, β_6, and β_8, β_9, which are shifted by b or $2b$ in the η direction. The oxygen anions β_3, β_6, and β_9 are above, while β_2, β_5, and β_8 are below the R-plane. Figure 9A also applies to the R'' plane, except that vacant interstitial sites from Figure 9A are occupied by aluminum cations.

Figure 9B shows the corresponding ionic distribution around the $R'(30\bar{3}6)$ plane. The oxygen anions α_2, α_4, α_7, $\beta 2$, β_5, and β_8 are above, while α_5, α_8, α_{11}, β_3, β_6, β_9, and β_{11} are below the $R'(30\bar{3}6)$ plane. Black circles are the aluminum cations within the R' plane. The oxygen anions nearest to the $r(1\bar{1}02)$ plane are shown in Figure 9C. The oxygen anions $\alpha_3(a/3, -2h/3, c/4)$, $\alpha_7(-a/6, -h/3, 7c/12)$, $\alpha_{11}(-2a/3, 0, 11c/12)$, $\beta_1(2a/3, -2h/3, c/12)$, $\beta_5(a/6, -h/3, 5c/12)$, and $\beta_9(-a/3, 0, 9c/12)$ are above, while $\alpha_4(a/3, 0, c/4)$, $\alpha_8(-a/6, h/3, 7c/12)$,

$\alpha_{12}(-2a/3, 2h/3, 11c/12)$, $\beta_2(2a/3, 0, c/12)$, $\beta_6(a/6, h/3, 5c/12)$, and $\beta_{10}(-a/3, 2h/3, 9c/12)$ are below the r-plane, all being at a normal distance of 0.58 Å from that plane. Because the ionic radius of the oxygen anion is $R_{O^{2-}} = 1.38$ Å, the oxygen anions with their centers at the distance 0.58 Å from the r-plane partly overlap with that plane.

For the sake of comparison, the oxygen anions closest to the $A(11\bar{2}0)$ plane are at $h_0/3 = a/6 = 0.793$ Å from that plane. The oxygen anions and aluminum cations closest to the $M(\bar{1}010)$ plane are both at $h/3 = a_0/2 = 1.374$ Å from that plane. Finally, as discussed in Section 1, the oxygen anions closest to the $C(0001)$ plane are at $c_0/2 = c/6 = 2.164$ Å from that plane, while the closest aluminum cations are at $c_0/4 = c/12 = 1.083$ Å from that plane (Figures 1 and 2). In addition to elastic properties and the length of the dislocation Burgers vector, the interplanar spacing between the slip planes and the proximity of the nearest ions to the slip plane affect most dominantly the magnitude of the lattice friction (Peierls) stress, which must be exceeded by the local Peach–Koehler force from the applied stress to drive dislocation and produce plastic deformation by crystallographic slip.[61–65] For example, the Peierls stress for the basal slip is lower than for the rhombohedral slip, because the interplanar spacing is greater and the nearby ions are more distant from the slip plane in the former case.

3 | $\Sigma(20\bar{2}4)$ PLANE

The $\Sigma(20\bar{2}4)$ plane is parallel to the R-plane and is located exactly in between the R' and R'' planes. It is a distinct crystallographic plane of sapphire, because it does not contain any aluminum cations or vacant interstitial sites, passing through the centers of oxygen anions only (Figure 10A). The equation of this plane in the (x, y, z) coordinate system is $2x/a + y/h + 4z/c = 1$, having the unit normal vector $\mathbf{n}_\Sigma = \{0.7313, 0.4222, 0.5356\}$, same as the R-plane. The Σ-plane is parallel to the a_2 axis, intersecting the a_1 axis at $a/2$, and the z-axis at $c/4$. Within the oxygen basal layer A ($z = -c/12$), the Σ-plane intersects the axes a_1^0 and a_2^0 at $a_0/2$, thus the Miller–Bravais indices of this plane with respect to the rotated hexagonal axes (a_1^0, a_2^0, a_3^0) are $\Sigma_0(2\bar{1}\bar{1}2)$. The corresponding equation in the coordinates system (x^0, y^0, z^0), with the origin in the center of the oxygen hexagon in the layer A, is obtained by using the coordinate transformation $x^0 = x - a/3$, $y^0 = y$, and $z^0 = z + c/12$, which gives $3x^0/(2h_0) + y^0/a_0 + 2z^0/c_0 = 1$, where $h_0 = \sqrt{3}a_0/2$, $a_0 = a/\sqrt{3}$, and $c_0 = c/3$ (Figures 1 and 5). The Σ-plane passes through oxygen anions from the A-layers shown in Figure 10B, whose (x^0, y^0, z^0) coordinates are $\alpha_1(h_0, -a_0/2, 0)$, $\alpha_3(0, -a_0, c_0)$, $\alpha_5(0, a_0, 0)$, $\alpha_6(-h_0, -3a_0/2, 2c_0)$, $\alpha_8(-h_0, a_0/2, c_0)$, $\alpha_{11}(-2h_0, 0, 2c_0)$, $\alpha_1'(-2h_0, -2a_0, 3c_0)$, and $\alpha_5'(-3h_0, -a_0/2, 3c_0)$. It also passes through oxygen anions from the B-layers whose coordinates are $\beta_6(-h_0/3, a_0/2, c_0/2)$, $\beta_9(-4h_0/3, 0, 3c_0/2)$, and $\beta_{11}(-7h_0/3, -a_0/2, 5c_0/2)$. The planar density of oxygen anions in the Σ-plane is $2/(ab) = 8.2/\text{nm}^2$. The close-packed direction of oxygen anions within the $\Sigma(20\bar{2}4)$ plane is the direction $[\bar{1}2\bar{1}0]$ (from α_1 to α_5), with the anion separation distance $a = 2h_0 = 4.758$ Å, which is $\sqrt{3}$ times greater than the shortest oxygen anion distance in a closed-packed oxygen layer A or B ($z = \mp c/12$).

The normal distance from the vacant interstitial site at a_6 (the origin of the (x, y, z) coordinate system) to the $\Sigma(20\bar{2}4)$ plane is 1.74 Å, while the normal distance from the oxygen anion at α_4 (the origin of the (x^0, y^0, z^0) coordinate system) to the $\Sigma_0(2\bar{1}\bar{1}2)$ plane is 1.16 Å, which is 2/3 times the distance 1.74 Å. The former is obtained from (2.3) with $h = 2$, $k = 0$, $l = 4$, $a = 4.758$ Å, and $c = 12.992$ Å, while the latter follows from (2.3) with $h = 2$, $k = -1$, $l = 2$, and the lattice parameters $a_0 = a/\sqrt{3}$ and $c_0 = c/3$. It is also noted that the dot product $\overrightarrow{a_6\alpha_4} \cdot \vec{n}_\Sigma = 0.58$ Å, which is the difference $(1.74 - 1.16)$ Å.

It is of interest to identify the aluminum cations nearest to the Σ-plane. By geometric considerations, details of which are omitted, it follows that the centers of the nearest aluminum cations have the following (x, y, z) coordinates: $\text{a}_3(a/2, h/, 0)$, $\text{a}_4(a/2, -h/3, 0)$, $\text{b}_4(a/2, -h/3, c/6)$, $\text{b}_6(0, 0, c/6)$, $\text{c}_6(0, 0, c/3)$, $\text{c}_7(0, -2h/3, c/3)$, $\hat{\text{a}}_7(0, -2h/3, c/2)$, $\hat{\text{a}}_9(-a/2, -h/3, c/2)$, $\hat{\text{b}}_9(-a/2, -h/3, 2c/3)$, $\hat{\text{b}}_{10}(-a/2, -h, 2c/3)$, $\hat{\text{c}}_{10}(-a/2, -h, 5c/6)$, and $\hat{\text{c}}_3'(-a, -2h/3, 5c/6)$. The corresponding (ξ, η) coordinates of the projected centers of these cations onto the Σ-plane are $\text{a}_3(2a/3, 0.1782b)$, $\text{a}_4(a/6, 0.3218b)$, $\text{b}_4(a/6, 0.6782b)$, $\text{b}_6(2a/3, 0.8218b)$, and likewise for other cations shown in Figure 11A. The aluminum cations $\text{a}_3, \text{b}_4, \text{c}_6, \hat{\text{a}}_7, \hat{\text{b}}_9$, and $\hat{\text{c}}_{10}$ are above, while $\text{a}_4, \text{b}_6, \text{c}_7, \hat{\text{a}}_9, \hat{\text{b}}_{10}$, and $\hat{\text{c}}_3'$ are below the $\Sigma(20\bar{2}4)$ plane, all being at the normal distance from it equal to 0.58 Å. The cations above the Σ plane are within the plane $3x/(2a) + 3y/(4h) + 3z/c = 1$ (R''-plane), while the cations below the Σ-plane are within the plane $3x/a + 3y/(2h) + 6z/c = 1$ (R'-plane). Because the ionic radius of the aluminum cation is $R_{Al^{3+}} = 0.57$ Å, the aluminum cations with their centers at the distance 0.58 Å from the Σ-plane are essentially tangent to that plane.

3.1 | $\sigma(2\bar{2}04)$ plane

The $\sigma(2\bar{2}04)$ plane is conjugate to the $\Sigma(20\bar{2}4)$ plane in the sense that it also passes through oxygen anions only, without passing through the centers of any

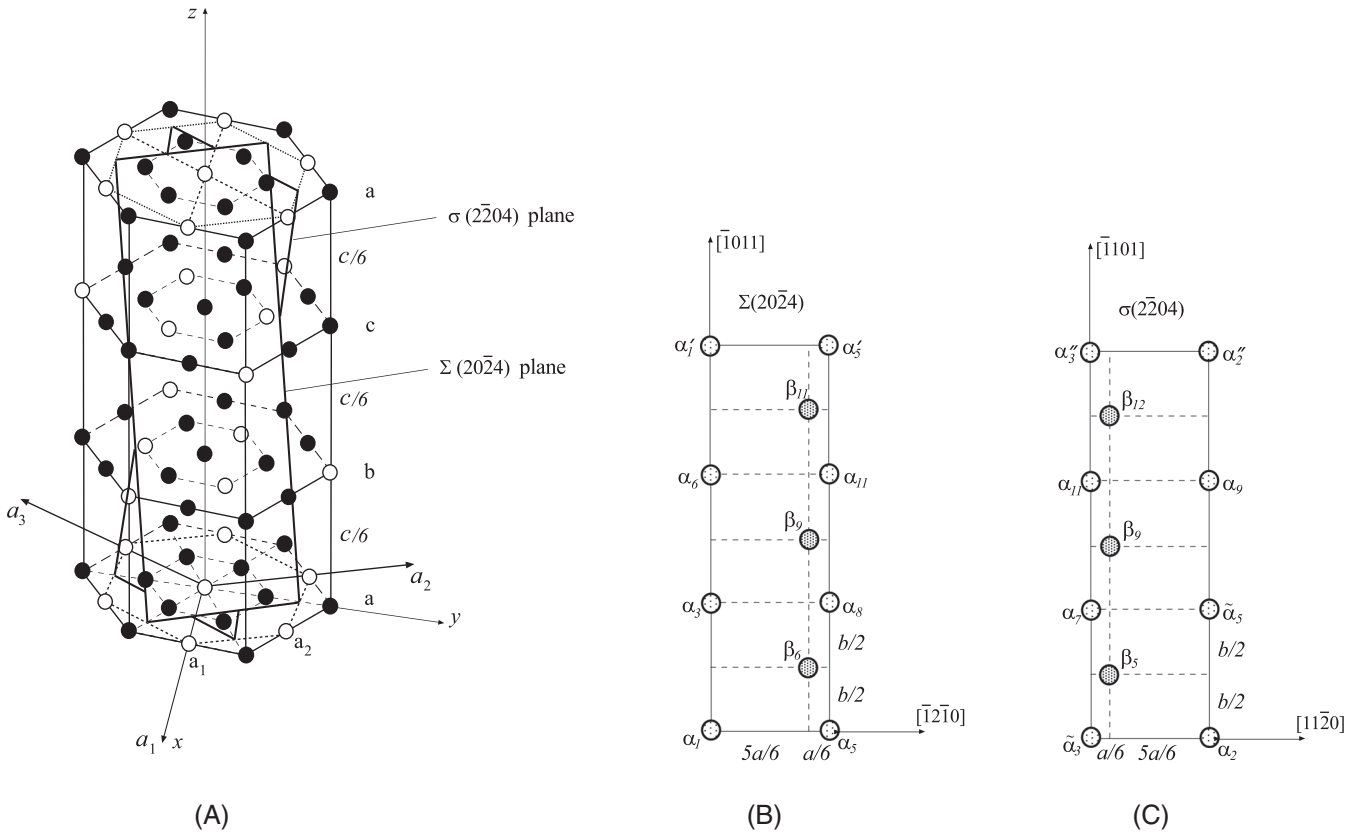

FIGURE 10 (A) The $\Sigma(20\bar{2}4)$ plane, intersecting the z-axis at $c/4$, the a_1 axis at $a/2$, and being parallel to the a_2 axis, does not contain any aluminum cations. Shown also is the adjacent $\sigma(2\bar{2}04)$ plane. (B) The segment of the $\Sigma(20\bar{2}4)$ plane passing through the centers of oxygen anions at α_1, α_5, α_3, α_8, α_6, α_{11}, α_1', and α_5' from the oxygen A-layers, and β_6, β_9, and β_{11} from the oxygen B-layers. (C) The segment of the $\sigma(2\bar{2}04)$ plane passing through the centers of oxygen anions at α_3', α_2, α_7, α_5', α_{11}, α_9, α_3'', and α_2'' from the oxygen A-layers, and β_5, β_9, and β_{12} from the oxygen B-layers.

aluminum cations or vacant interstitial sites. It is precisely in between the r' and r'' planes, introduced in Section 2. The centers of oxygen anions from the A-layers belonging to the σ plane (Figure 10C) have their (x^0, y^0, z^0) coordinates: $\alpha_2(h_0, a_0/2, 0)$, $\tilde{\alpha}_3(0, -a_0, 0)$, $\tilde{\alpha}_5(0, a_0, c_0)$, $\alpha_7(-h_0, -a_0/2, c_0)$, $\alpha_9(-h_0, 3a_0/2, 2c_0)$, $\alpha_{11}(-2h_0, 0, 2c_0)$, $\alpha_2''(-2h_0, 2a_0, 3c_0)$, and $\alpha_3''(-3h_0, a_0/2, 3c_0)$. The coordinates of oxygen anions from the B-layers are $\beta_5(-h_0/3, -a_0/2, c_0/2)$, $\beta_9(-4h_0/3, 0, 3c_0/2)$, and $\beta_{12}(-7h_0/3, a_0/2, 5c_0/2)$. The planar density of oxygen anions within σ plane is the same as within Σ plane ($8.2/\text{nm}^2$). The equation of σ plane in the (x, y, z) coordinate system is $2x/a - y/h + 4z/c = 1$, with the corresponding representation in the (x^0, y^0, z^0) system given by $3x^0/(2h_0) - y^0/a_0 + 2z^0/c_0 = 1$. The superimposed $\tilde{}$ is used to indicate a different z_0 coordinate in $\alpha_3(0, -a_0, c_0)$ and $\tilde{\alpha}_3(0, -a_0, 0)$, and likewise in $\alpha_5(0, a_0, 0)$ and $\tilde{\alpha}_5(0, a_0, c_0)$.

The centers of nearest aluminum cations (black circles), or vacant interstitial sites (open circles) have the (x, y, z) coordinates: $a_3(a/2, h/3, 0)$, $b_3(a/2, h/3, c/6)$, $a_4(a/2, -h/3, 0)$, $c_5(0, 2h/3, c/3)$, $\hat{a}_5(0, 2h/3, c/2)$, $b_6(0, 0, c/6)$, $c_6(0, 0, c/3)$, $\hat{a}_8(-a/2, h/3, c/2)$, $\hat{b}_8(-a/2, h/3, 2c/3)$, $\hat{b}_{12}(-a/2, h, 2c/3)$, $\hat{c}_{12}''(-a/2, h, 5c/6)$, and $\hat{c}_4''(-a, 2h/3, 5c/6)$. The corresponding (ξ, η) coordinates of the projected centers of these cations onto the σ plane are $a_4(a/3, 0.1782b)$, $a_3(5a/6, 0.3218b)$, $b_3(5a/6, 0.6782b)$, $b_6(a/3, 0.8218b)$, and likewise for other cations shown in Figure 11B. The aluminum cations or vacant interstitial sites $b_3, a_4, \hat{a}_5, c_6, \hat{b}_8$, and $\hat{c}_{12}''$ are above, while $a_3, c_5, b_6, \hat{a}_8, \hat{b}_{12}$, and $\hat{c}_4''$ are below the $\sigma(2\bar{2}04)$ plane, all being at the normal distance from it equal to 0.58 Å. The cations above the σ-plane are within the plane $3x/(2a) - 3y/(4h) + 3z/c = 1$ (r''-plane), while the cations below the σ-plane are within the plane $3x/a - 3y/(2h) + 6z/c = 1$ (r'-plane), both being parallel to the σ-plane.

Because of the absence of 60° rotational symmetry of the α-Al_2O_3 corundum structure, ionic distributions within and around $\Sigma(20\bar{2}4)$ and $\sigma(2\bar{2}04)$ planes are different. While in Figure 11B both aluminum cations and vacant interstitial sites are present nearby the $\sigma(2\bar{2}04)$ plane, there are no vacant interstitial sites nearby the $\Sigma(20\bar{2}4)$ plane shown in Figure 11A.

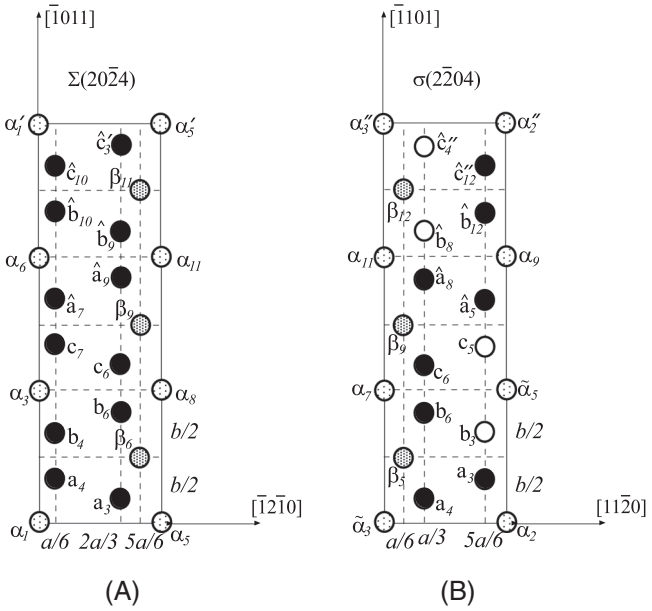

FIGURE 11 (A) The aluminum cations (black circles) $a_3, b_4, c_6, \hat{a}_7, \hat{b}_9$, and $\hat{c}_{10}$ are below, while $a_4, b_6, c_7, \hat{a}_9, \hat{b}_{10}$, and $\hat{c}'_3$ are above the $\Sigma(20\bar{2}4)$ plane, all being at the normal distance from it equal to 0.58 Å. (B) The aluminum cations $a_4, \hat{a}_5, c_6$ and $\hat{c}''_{12}$, and the vacant interstitial sites b_3 and $\hat{b}_8$ are above, while the cations $a_3, b_6, \hat{a}_8$ and $\hat{b}_{12}$, and the vacant interstitial sites c_5 and $\hat{c}''_4$ are below the $\sigma(2\bar{2}04)$ plane, all being at the normal distance from it equal to 0.58 Å.

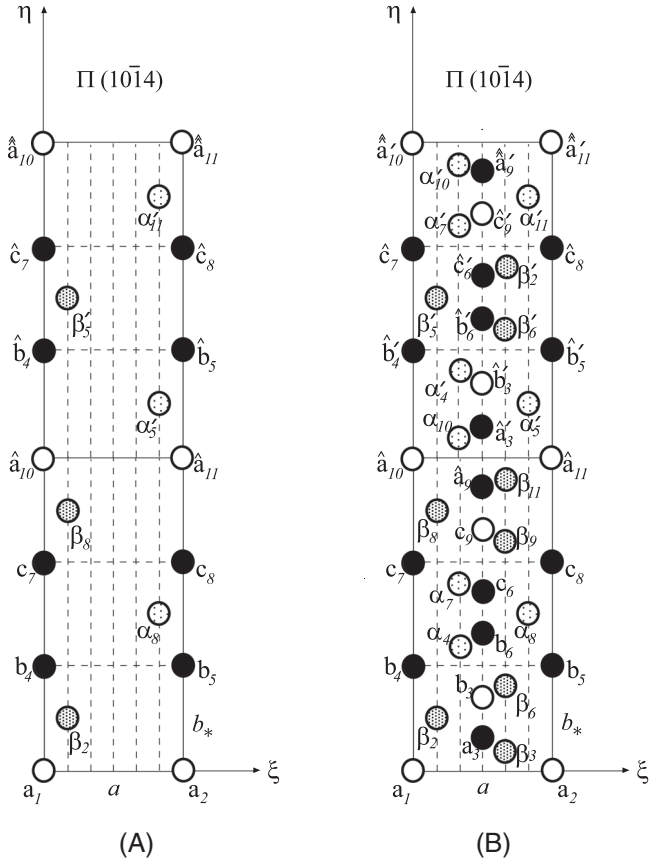

FIGURE 12 (A) The segment of the $\Pi(10\bar{1}4)$ plane passing through the vacant interstitial sites (open circles), and through the centers of aluminum cations (black circles). The oxygen anions at $\alpha_8, \alpha'_5, \alpha'_{11}, \beta_2, \beta_8$, and β'_5 are also within the Π-plane. (B) Same as in part (A), but with added projections of the centers of oxygen anions and aluminum cations nearest to the $\Pi(10\bar{1}4)$ plane. The oxygen anions $\alpha_4, \alpha_{10}, \alpha'_7, \beta_3, \beta_9$, and β'_6 are above, while $\alpha_7, \alpha'_4, \alpha'_{10}, \beta_6, \beta_{11}$, and β'_2 are below the Π-plane, all being at the normal distance 0.85 Å from the Π-plane. The aluminum cations c_6, $\hat{a}_9$, $\hat{c}'_6$, and $\hat{a}'_9$ are above the Π-plane, while a_3, b_6, $\hat{a}'_3$, and $\hat{b}'_6$ are below the Π-plane, all being at the normal distance $d_\Pi/2 = 0.85$ Å from the Π-plane. The interplanar distance between two adjacent Π-planes is $d_\Pi = 1.7$ Å.

4 | Π(10$\bar{1}$4) PLANE

The $\Pi(10\bar{1}4)$ plane is an analog to the *R*-plane with respect to the morphological rather than structural unit cell (Figure 6B). It passes through interstitial sites a_1, a_2, b_4, b_5, c_7, and c_8, whose (x, y, z) coordinates are specified in the caption of Figure 3, and through points $\hat{a}_{10}(-a/2, -h, c/2)$ and $\hat{a}_{11}(-a, 0, c/2)$, thus having the equation $x/a + y/(2h) + 4z/c = 1$. The interstitial sites a_1, a_2, a_{10}, and a_{11} are vacant, while b_4, b_5, c_7, and c_8 are occupied by aluminum cations. The centers of oxygen anions with (x, y, z) coordinates $\alpha_8(-a/6, h/3, c/4)$, $\alpha'_5(-7a/6, -h/3, 7c/12)$, $\alpha'_{11}(-13a/6, -h, 11c/12)$, $\beta_2(2a/3, 0, c/12)$, $\beta_8(-a/3, -2h/3, 5c/12)$, and $\beta'_5(-4a/3, -4h/3, 3c/4)$ are also within the $\Pi(10\bar{1}4)$ plane (Figure 12A). The attached prime ($'$) is used to indicate that α'_5, α'_{11}, and β'_5 are behind the hexagon shown in Figure 5, in the direction $-a_1^0$. The corresponding (ξ, η) coordinates of the oxygen centers within the Π-plane are $\alpha_8(5a/6, 1.5b_*)$, $\alpha'_5(5a/6, 3.5b_*)$, $\alpha'_{11}(5a/6, 5.5b_*)$, $\beta_2(a/6, 0.5b_*)$, $\beta_8(a/6, 2.5b_*)$, and $\beta'_5(a/6, 4.5b_*)$. The distance from the coordinate origin within the cation *a*-layer (Figure 6B) to the point b_5 within the cation *b*-layer is equal to $b_* = [(2h/3)^2 + (c/6)]^2 = 3.498$ Å, the length of the edge of the smallest morphological rhombohedral cell (of height $c/2$), which embeds two consecutive aluminum cations along the *z*-direction (at $z = c/6$ and $z = c/3$). The unit vector orthogonal to the Π-plane is $\mathbf{n}_\Pi = \{0.5361, 0.3095, 0.7854\}$, which makes an angle of 38.24° with the *z*-axis. The normal distance between two adjacent Π-planes is $d_\Pi = 1.7$ Å. The planar density of vacant interstitial sites within the Π-plane is $1/(3ab_*) = 2/\text{nm}^2$, the planar density of aluminum cations is $2/(3ab_*) = 4/\text{nm}^2$, and the planar density of oxygen anions is $3/(3ab_*) = 6/\text{nm}^2$.

The centers of oxygen anions from the *A*-layers at $\alpha_4(a/3, 0, c/4)$, $\alpha_7(-a/6, -h/3, c/4)$, $\alpha_{10}(-2a/3, -2h/3, 7c/12)$, $\alpha'_4(-7a/6, -h, 7c/12)$, $\alpha'_7(-5a/3, -4h/3, 11c/12)$, and $\alpha'_{10}(-13a/6, -5h/3, 11c/12)$, and the centers of

oxygen anions from the B-layers at $\beta_3(2a/3, 2h/3, c/12)$, $\beta_6(a/6, h/3, 5c/12)$, $\beta_9(-a/3, 0, 5c/12)$, $\beta_{11}(-5a/6, -h/3, 5c/12)$, $\beta'_6(-4a/3, -2h/3, 3c/4)$, and $\beta'_2(-11a/6, -h, 3c/4)$ are all at the normal distance $d_\Pi/2 = 0.85$ Å from the Π plane. The oxygen anions α_4, α_{10}, α_{16}, β_3, β_9, and β'_6 are below, while α_7, α'_4, α'_{10}, β_6, β_{11}, and β'_2 are above the Π plane. The (ξ, η) coordinates of the projected centers of eight oxygen anions onto the Π plane are $\alpha_4(a/3, 1.192b_*)$, $\alpha_7(a/3, 1.808b_*)$, $\alpha_{10}(a/3, 3.192b_*)$, $\alpha'_4(a/3, 3.808b_*)$, $\alpha'_7(a/3, 5.192b_*)$, $\alpha'_{10}(a/3, 5.808b_*)$, $\beta_3(2a/3, 0.192b_*)$, $\beta_6(2a/3, 0.808b_*)$, $\beta_9(2a/3, 2.192b_*)$, $\beta_{11}(2a/3, 2.808b_*)$, $\beta'_6(2a/3, 4.192b_*)$, and $\beta'_2(2a/3, 4.808b_*)$, as shown in Figure 12B. The aluminum cations at a_3, b_6, c_6, $\hat{a}_9(-a/2, -h/3, c/2)$, $\hat{a}'_3(-a, -2h/3, c/2)$, $\hat{b}'_6(-3a/2, -h, 2c/3)$, $\hat{c}'_6(-3a/2, -h, 5c/6)$, and $\hat{a}'_9(-2a, -4h/3, c)$ are also at a normal distance of 0.85 Å from the Π-plane. The aluminum cations a_3, b_6, $\hat{a}'_3$, and $\hat{b}'_6$ are below the Π-plane, belonging to the $\Pi^-(30\bar{3}12)$ plane whose equation is $3x/(2a) + 3y/(4h) + 6z/c = 1$, while aluminum cations c_6, $\hat{a}_9$, $\hat{c}'_6$, and $\hat{a}'_9$ are above the Π-plane, belonging to the $\Pi^+(30\bar{3}12)$ plane whose equation is $3x/(2a) + 3y/(4h) + 6z/c = 2$. The (ξ, η) coordinates of the projected centers of aluminum cations a_3 and c_6 onto the Π plane are $(0.5a, 0.3084b_*)$ and $(0.5a, 1.6916b_*)$, and likewise for other cations shown in Figure 12B. The normal distance between the planes Π^- and Π^+ is $(m^2 + n^2 + p^2)^{-1/2} = 1.7$ Å, where $m = 3/(2a)$, $n = 3/(4h)$, and $p = 6/c$, as expected because the Π-plane is exactly midway between the Π^- and Π^+ planes, which are both at 0.85 Å from the Π-plane. Because the ionic radii of the oxygen anion and aluminum cation are 1.38 Å and 0.57 Å, respectively, the oxygen anions with their centers at the distance 0.85 Å from the Π-plane partly overlap with that plane, while the aluminum cations with their centers at the distance 0.85 Å from the Π-plane do not overlap with that plane.

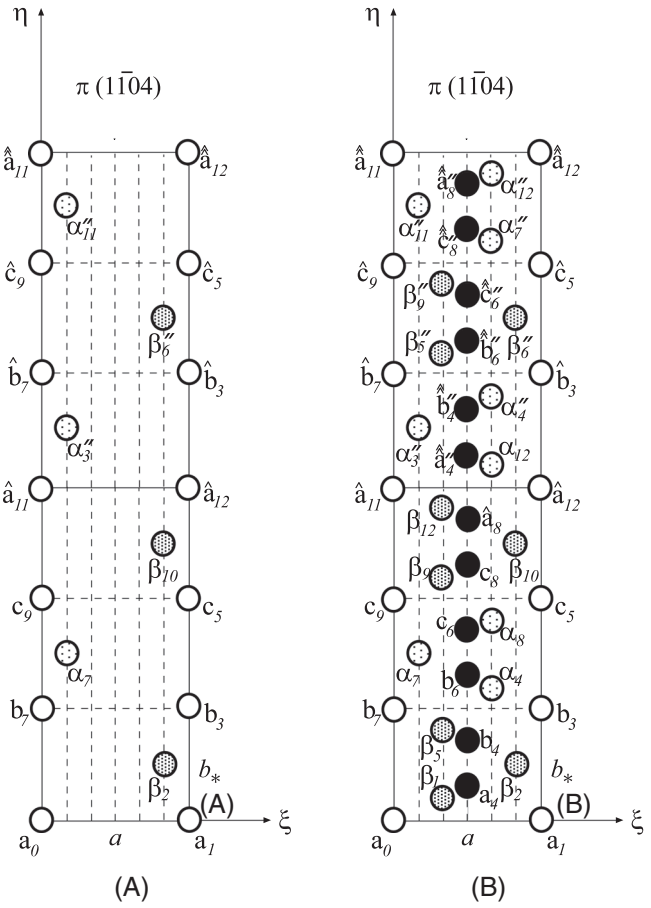

FIGURE 13 (A) The segment of the $\pi(1\bar{1}04)$ plane passing through the vacant interstitial sites (open circles). The oxygen anions at α_7, α''_3, α''_{11}, β_2, β_{10}, and β''_6 are also within the π-plane. (B) Same as in part (A), but with added projections of the centers of oxygen anions nearest to the $\pi(1\bar{1}04)$ plane. The oxygen anions α_4, α_{12}, α''_7, β_1, β_9, and β''_5 are above, while α_8, α''_4, α''_{12}, β_5, β_{12}, and β''_9 are above the π-plane, all being at the normal distance 0.85 Å from the π-plane. The aluminum cations b_4, c_6, $\hat{a}_8$, $\hat{b}''_4$, $\hat{c}''_6$, and $\hat{a}''_8$ are above the π-plane, while a_4, b_6, c_8, $\hat{a}''_4$, $\hat{b}''_6$, and $\hat{c}''_8$ are below the π-plane, all being at the normal distance $d_\pi/2 = 0.85$ Å from the π-plane. The interplanar distance between two adjacent π-planes is $d_\pi = 1.7$ Å.

4.1 | $\pi(1\bar{1}04)$ plane

The $\pi(1\bar{1}04)$ plane passes through vacant interstitial sites a_0, a_1, b_7, b_3, c_9, and c_5, whose (x, y, z) coordinates are specified in the caption of Figure 3, and through points $\hat{a}_{11}$, $\hat{a}_{12}$, $\hat{b}_7$, $\hat{b}_3$, $\hat{c}_9$, and $\hat{c}_5$, vertically shifted by $c/2$ (e.g., $\hat{a}_{11}(-a, 0, c/2)$ and $\hat{a}_{12}(-a/2, h, c/2)$), thus having the equation $x/a - y/(2h) + 4z/c = 1$. The coordinates of the remaining two vacant interstitial sites are $\hat{a}_{11}(-a, 0, c)$ and $\hat{a}_{12}(-a/2, h, c)$. The centers of oxygen anions with (x, y, z) coordinates $\alpha_7(-a/6, -h/3, c/4)$, $\alpha''_3(-7a/6, h/3, 7c/12)$, $\alpha''_{11}(-13a/6, h, 11c/12)$, $\beta_2(2a/3, 0, c/12)$, $\beta_{10}(-a/3, 2h/3, 5c/12)$, and $\beta''_6(-4a/3, 4h/3, 3c/4)$ are also within the $\pi(1\bar{1}04)$ plane (Figure 13A). The attached double-prime ($''$) is used to indicate that α''_3, α''_{11}, and β''_6 are behind the hexagon shown in Figure 5, in the direction a_2^0. The corresponding (ξ, η) coordinates of the oxygen centers within the π-plane are $\alpha_7(a/6, 1.5b_*)$, $\alpha''_3(a/6, 3.5b_*)$, $\alpha''_{11}(a/6, 5.5b_*)$, $\beta_2(5a/6, 0.5b_*)$, $\beta_10(5a/6, 2.5b_*)$, and $\beta''_6(5a/6, 4.5b_*)$. The unit vector orthogonal to the π-plane is $\mathbf{n}_\pi = \{0.5361, -0.3095, 0.7854\}$. The normal distance between two adjacent π-planes is $d_\pi = 1.7$ Å. The planar densities of vacant interstitial sites and aluminum cations within the π-plane are the same as those within the Π-plane.

The centers of oxygen anions from the A-layers at $\alpha_4(a/3, 0, c/4)$, $\alpha_8(-a/6, h/3, c/4)$, $\alpha_{12}(-2a/3, 2h/3, 7c/$

12), $\alpha_4''(-7a/6, h, 7c/12)$, $\alpha_7''(-5a/6, 4h/3, 11c/12)$, and $\alpha_{12}''(-13a/6, 5h/3, 11c/12)$, and the centers of oxygen anions from the B-layers at $\beta_1(2a/3, -2h/3, c/12)$, $\beta_5(a/6, -h/3, c/12)$, $\beta_9(-a/3, 0, 5c/12)$, $\beta_{12}(-5a/6, h/3, 5c/12)$, $\beta_5''(-4a/3, 2h/3, 3c/4)$, and $\beta_9''(-11a/6, h, 3c/4)$ are at the normal distance $d_\pi/2 = 0.85$ Å from the π-plane. The oxygen anions α_4, α_{12}, α_7'', β_1, β_9, and β_5'' are above, while α_8, α_4'', α_{12}'', β_5, β_{12}, and β_9'' are below the π-plane. The (ξ, η) coordinates of the projected centers of eight oxygen anions onto the π-plane are $\alpha_7(a/6, 1.5b_*)$, $\alpha_4(2a/3, 1.192b_*)$, $\alpha_8(2a/3, 1.808b_*)$, $\alpha_3''(a/3, 3.5b_*)$, $\alpha_{12}(2a/3, 3.192b_*)$, $\alpha_4''(2a/3, 3.808b_*)$, $\alpha_{11}''(a/6, 5.5b_*)$, $\alpha_7''(2a/3, 5.192b_*)$, $\alpha_{12}''(2a/3, 5.808b_*)$, $\beta_1(a/3, 0.192b_*)$, $\beta_5(a/3, 0.808b_*)$, $\beta_2(5a/6, 0.5b_*)$, $\beta_9(a/3, 2.192b_*)$, $\beta_{12}(a/3, 2.808b_*)$, $\beta_{10}(5a/6, 2.5b_*)$, $\beta_5''(a/3, 4.192b_*)$, $\beta_9''(a/3, 4.808b_*)$, $\beta_6''(5a/6, 4.5b_*)$, which is shown in Figure 13B. The aluminum cations at a_4, b_4, b_6, c_6, c_8, $\hat{a}_8(-a/2, h/3, c/2)$, $\hat{a}_4''(-a, 2h/3, c/2)$, $\hat{b}_4''(-a, 2h/3, 2c/3)$, $\hat{b}_6''(-3a/2, h, 2c/3)$, $\hat{c}_6''(-3a/2, h, 5c/6)$, $\hat{c}_8''(-2a, 4h/3, 5c/6)$, and $\hat{a}_8''(-2a, 4h/3, c)$ are also at a normal distance of 0.85 Å from the π-plane. The aluminum cations a_4, b_6, c_8, $\hat{a}_4''$, $\hat{b}_6''$, and $\hat{c}_8''$ are below the π-plane, belonging to the $\pi^-(3\bar{3}012)$ plane whose equation is $3x/(2a) - 3y/(4h) + 6z/c = 1$, while aluminum cations b_4, c_6, $\hat{a}_8$, $\hat{b}_4''$, $\hat{c}_6''$, and $\hat{a}_8''$ are above the π-plane, belonging to the $\pi^+(3\bar{3}012)$ plane whose equation is $3x/(2a) - 3y/(4h) + 6z/c = 2$. The (ξ, η) coordinates of the projected centers of aluminum cations onto the π-plane are $(0.5a, 0.3084b_*)$ and $(0.5a, 0.6916b_*)$, and likewise for other cations shown in Figure 13B. The normal distance between the planes π^- and π^+ is $(m^2 + n^2 + p^2)^{-1/2} = 1.7$ Å, where $m = 3/(2a)$, $n = -3/(4h)$, and $p = 6/c$. If diffusion of impurities is taking place within the ion-free π-plane, the aluminum cations and oxygen anions from the π^- and π^+ planes exert the strongest interaction forces on the diffusing impurities. Dislocation pipe diffusion along dislocation cores in ceramics has been discussed in reference.[48]

5 | CONCLUSION

The positions of aluminum and oxygen ions within and nearby several distinct crystallographic planes of the α-Al_2O_3 corundum structure have been determined and discussed. The considered planes are the $R(10\bar{1}2)$, $R'(30\bar{3}6)$, $\Sigma(20\bar{2}4)$, and $\Pi(10\bar{1}4)$ planes, and their adjacent planes $r(1\bar{1}02)$, $r'(3\bar{3}06)$, $\sigma(2\bar{2}04)$, and $\pi(1\bar{1}04)$. The $R(10\bar{1}2)$ plane contains neither aluminum nor oxygen ions, while $\Sigma(20\bar{2}4)$, $\sigma(20\bar{2}4)$, and $\pi(1\bar{1}04)$ planes contain only oxygen anions, whose planar densities are $\rho_\pi = 6/\text{nm}^2$ and $\rho_\Sigma = \rho_\sigma = 8.2/\text{nm}^2$. The $R'(30\bar{3}6)$, $r'(3\bar{3}06)$, and $r(1\bar{1}02)$ planes contain only aluminum cations with planar densities $\rho_{R'} = 8.2/\text{nm}^2$ and $\rho_r = \rho_{r'} = 5.47/\text{nm}^2$. The $\Pi(10\bar{1}4)$ plane contains both aluminum and oxygen ions, with planar densities $\rho_\Pi^{Al} = 4/\text{nm}^2$ and $\rho_\Pi^{O} = 6/\text{nm}^2$. It is also shown that the nearest ions to the $R(10\bar{1}2)$, $r(1\bar{1}02)$, $R'(30\bar{3}6)$, $r'(3\bar{3}06)$, $\Sigma(20\bar{2}4)$, and $\sigma(2\bar{2}04)$ planes are at the normal distance 0.58 Å from these planes, while the nearest ions to the $\Pi(10\bar{1}4)$ and $\pi(1\bar{1}04)$ planes are at 0.85 Å from these planes. The presented analysis and obtained results are of potential interest for analytical and computational studies of plastic deformation of sapphire crystals produced by dislocation slip or twinning, cleavage fracture over different crystallographic planes under different loading, strain rates, and temperature, impurity diffusion along interstitial pathways and corresponding clustering of impurity atoms such as chromium, diffusion creep, evaluation of surface, stacking and electrostatic fault energies, twin interface energy, and the growth of thin films over differently oriented sapphire substrates with applications to microelectronic, LED, and other devices. The obtained results may also help the development or extension of existing algorithms and computer software for the analysis of complex crystalline structures and systems.

ACKNOWLEDGEMENTS

Helpfulful comments and suggestions by the reviewers are gratefully acknowledged.

CONFLICTS OF INTEREST

The authors declare that there is no conflict of interest that could be perceived as prejudicing the impartiality of the research reported.

ORCID

Vlado A. Lubarda https://orcid.org/0000-0002-0474-6681

Marko V. Lubarda https://orcid.org/0000-0002-3755-271X

REFERENCES

1. Pauling L, Hendricks SB. The crystal structures of hematite and corundum. J Am Chem Soc. 1925;47(3):781–90. https://doi.org/10.1021/ja01680a027
2. Kronberg ML. Plastic deformation of single crystals of sapphire: basal slip and twinning. Acta Metal. 1957;5(9):507–27. https://doi.org/10.1016/0001-6160(57)90090-1
3. Levin I, Brandon D. Metastable alumina polymorphs: crystal structures and transition sequences. J Amer Ceram Soc. 1998;81(8):1995–2012. https://doi.org/10.1111/j.1151-2916.1998.tb02581.x
4. Lee WE, Lagerlof KPD. Structural and electron diffraction data for sapphire (α-Al_2O_3). J Elec Micros Tech. 1985;2(3):247–58. https://doi.org/10.1002/jemt.1060020309
5. Hyde BG, Andersson S. Inorganic crystal structures. New York: Wiley; 1989.

6. Al-Abadleh HA, Grassian VH. Oxide surfaces as environmental interfaces. Surf Sci Rep. 2003;52(3–4):63–161. https://doi.org/10.1016/j.surfrep.2003.09.001
7. Newnham RE, de Haan YM. Refinement of the Al_2O_3, Ti_2O_3, V_2O_3, and Cr_2O_3 structures. Z Krist. 1962;117(1–6):235–37. https://doi.org/10.1524/zkri.1962.117.16.235
8. Dobrovinskaya ER, Lytvynov LA, Pishchik V. Properties of sapphire. In: Dobrovinskaya ER et al., editors. Sapphire—material, manufacturing, applications. New York: Springer; 1970. p. 55–176. https://doi.org/10.1007/978-0-387-85695-7_2
9. Wyckoff RWG. Crystal structures, vol. 2, 2nd ed. New York: Interscience; 1963.
10. Han T, editor,. International tables for crystallography, space group symmetry, vol. A, 5th ed. New York: Wiley; 2005.
11. Kelly A, Knowles KM. Crystallography and crystal defects, 2nd ed. New York: Wiley; 2012.
12. Malgrange C, Ricolleau C, Schlenker M. Symmetry and physical properties of crystals. Dordrecht: Springer; 2014. https://doi.org/10.1007/978-94-017-8993-6
13. Özgür Ü, Avrutin V, Morkoç H. Zinc oxide materials and devices grown by molecular beam epitaxy. In: Henini M, editor. Molecular beam epitaxy: from research to mass production, 2nd ed. Amsterdam: Elsevier; 2018. p. 343–75. https://doi.org/10.1016/B978-0-12-812136-8.00016-5
14. Wen Q, Zhang P, Cheng G, Jiang F, Lu X. Crystalline orientation effects on material removal of sapphire by femtosecond laser irradiation, Ceram Int. 2019;45(17):23501–08. https://doi.org/10.1016/j.ceramint.2019.08.056
15. Roder C, Einfeldt S, Figge S, Paskova T, Hommel D, Paskov PP, et al. Stress and wafer bending of *a*-plane GaN layers on *r*-plane sapphire substrates. J Appl Phys. 2006;100(10):103511. https://doi.org/10.1063/1.2386940
16. Guo J, Ellis DE, Lam DJ. Electronic structure and energetics of sapphire (0001) and ($1\bar{1}02$) surfaces. Phys Rev B. 1992;45(23):13647. https://doi.org/10.1103/PhysRevB.45.13647
17. Ching WY, Xu Y-N. First-principles calculation of electronic, optical, and structural properties of α-Al_2O_3. J Am Ceram Soc. 1994;77(2):404–11. https://doi.org/10.1111/j.1151-2916.1994.tb07008.x
18. Kitayama M, Glaeser AM. The Wulff shape of alumina: III, Undoped alumina. J Am Ceram Soc. 2002;85(3):611–22. https://doi.org/10.1111/j.1151-2916.2002.tb00140.x
19. Bakholdin SI, Maslov VN. Simulation of surface energies of sapphire crystals. Phys Solid State. 2015;57(6):1236–43. https://doi.org/10.1134/S1063783415060037
20. Wildes AR, Mayer J, Theis-Bröhl K. The growth and structure of epitaxial niobium on sapphire. Thin Solid Films. 2001; 401(1–2):7–34. https://doi.org/10.1016/S0040-6090(01)01631-5
21. Craven MD, Lim SH, Wu F, Speck JS, DenBaars SP. Structural characterization of nonpolar ($11\bar{2}0$)*a*-plane GaN thin films grown on ($1\bar{1}02$)*r*-plane sapphire. Appl Phys Lett. 2002;81(3):469–71. https://doi.org/10.1063/1.1493220
22. Saha SK, Kumar R, Kuchuk A, Stanchu H, Mazur YI, Yu S-Q, et al. GaAs epitaxial growth on *R*-plane sapphire substrate, J Crystal Growth. 2020;548:125848. https://doi.org/10.1016/j.jcrysgro.2020.125848
23. Nakao W, Takahashi K, Ando K. Self-healing of surface cracks in structural ceramics. In: Ghosh SK, editor. Self-healing materials—fundamentals, design strategies, and applications. Weinheim, Germany: Wiley-VCH; 2009. p. 183–217.
24. Boatemaa L, Van der Zwaag S, Sloof WG. Self-healing of Al_2O_3 containing Ti microparticles. Ceram Int. 2018;44(10):11116–26.
25. Klassen-Neklyudova MV, Govorkov VG, Urusovskaya AA, Voinova NN, Kozlovskaya EP. Plastic deformation of corundum single crystals. Phys Status Solidi B. 1970;39(2):679–88. https://doi.org/10.1002/pssb.19700390236C
26. Snow JD, Heuer AH. Slip systems in A_2O_3. J Am Cheram Soc. 1973;56(3):153–7. https://doi.org/10.1111/j.1151-2916.1973.tb15432.x
27. Shibata N, Chisholm MF, Nakamura A, Pennycook SJ, Yamamoto T, Ikuhara Y. Nonstoichiometric dislocation cores in α-alumina. Science 2007;316(5821):82–5. https://doi.org/10.1126/science.1136155
28. Lagerlöf KPD, Castaing J, Heuer AH. Do moving basal dislocations in sapphire (α-Al_2O_3) have non-stoichiometric cores? Phil Mag. 2009;89(5):489–99. https://doi.org/10.1080/14786430802672691
29. Grundmann M, Stralk T, Lorenz M, Selle S, Patzig C, Höche T. Plastic strain relaxation and alloy instability in epitaxial corundum-phase (Al, Ga_2O_3) thin films on *r*-plane A_2O_3. Mater Adv. 2021;2(13):4316–22. https://doi.org/10.1039/d1ma00204j
30. Vodenitcharova T, Zhang LC, Zarudi I, Yinb Y, Domyoc H, Hoc T, Sato M. The effect of anisotropy on the deformation and fracture of sapphire wafers subjected to thermal shocks. J Mater Process Techn. 2007;194(1–3):52–62. https://doi.org/10.1016/j.jmatprotec.2007.03.125
31. Wang N, Jiang F, Xu X, Lu X. Effects of crystal orientation on the crack propagation of sapphire by sequential indentation testing. Crystals. 2018;8(1):1–13. https://doi.org/10.3390/cryst8010003
32. Tang H, Li H, Xu J. Growth and development of sapphire crystal for LED applications. In: Ferreira SO, editor. Advanced topics on crystal growth. Rijeka: InTech; 2013. p. 307–333. https://doi.org/10.5772/54249
33. Rao R, Pint CL, Islam AE, Weatherup RS, Hofmann S, Meshot ER, et al. Carbon nanotubes and related nanomaterials: critical advances and challenges for synthesis toward mainstream commercial applications. ACS Nano 2018;12(12):11756–84. https://doi.org/10.1021/acsnano.8b06511
34. Wiederhorn SM. Fracture of sapphire. J Amer Ceram Soc. 1969;52(9):485–91. https://doi.org/10.1111/j.1151-2916.1969.tb09199.x
35. Wiederhorn SM, Hockey BJ, Roberts DE. Effect of temperature on the fracture of sapphire. Phil Mag A. 1973;28(4):783–96, dio:10.1080/14786437308220983
36. Kingery WD, Bowen HK, Uhlmann DR. Introduction to ceramics, 2nd ed. New York: Wiley; 1976.
37. Kotchick DM, Tressler RE. Deformation behavior of sapphire via the prismatic slip system. J Am Ceram Soc. 1980;63(7–8):429–34. https://doi.org/10.1111/j.1151-2916.1980.tb10206.x
38. Cannon RM, Rhodes WH, Heuer AH. Plastic deformation of fine-grained alumina (Al_2O_3): I. Interface-controlled diffusional creep. J Am Ceram Soc. 1980;63(1–2):46–53. https://doi.org/10.1111/j.1151-2916.1980.tb10648.x
39. Heuer AH, Tighe NJ, Cannon RM. Plastic deformation of fine-grained alumina (Al_2O_3): II. Basal slip and nonaccommodated grain-boundary sliding. J Am Ceram Soc. 1980;63(1–2):53–8. https://doi.org/10.1111/j.1151-2916.1980.tb10649.x
40. Lagerlöf KPD, Heuer AH, Castaing J, Riviére JP, Mitchell TE. Slip and twinning in sapphire (α-Al_2O_3). J Am Ceram

Soc. 1994;77(2):385–97. https://doi.org/10.1111/j.1151-2916.1994.tb07006.x
41. Bilde-Sørensen JB, Lawlor BF, Geipel T, Pirouz P, Heuer AH, Lagerlöf KPD. On basal slip and basal twinning in sapphire (α-Al_2O_3)-I. Basal slip revisited. Acta Mater. 1996;44(5):2145–52. https://doi.org/10.1016/1359-6454(95)00264-2
42. Porz L. 60 years of dislocations in ceramics: a conceptual framework for dislocation mechanics in ceramics. Int J Ceram Eng Sci. 2022;4:214–39. https://doi.org/10.1002/ces2.10150
43. Bodur CT, Chang J, Argon AS. Molecular dynamics simulations of basal and pyramidal system edge dislocations in sapphire. J. Eur Ceram Soc. 2005;25(8):1431–39. https://doi.org/10.1016/j.jeurceramsoc.2005.01.022
44. Xu Q, Salles N, Chevalier J, Amodeo J. Atomistic simulation and interatomic potential comparison in α-Al_2O_3: lattice, surface and extended-defects properties. Model Simul Mat Sci Eng. 2022;30(3):035008. https://doi.org/10.1088/1361-651X/ac4d76
45. Chitnis A, Chen C, Adivarahan V, Shatalov M, Kuokstis E, Mandavilli V, Yang J, Khan MA. Visible light-emitting diodes using *a*-plane GaN–InGaN multiple quantum wells over *r*-plane sapphire. Appl Phys Lett. 2004;84(18):3663–5. https://doi.org/10.1063/1.1738938
46. Zhao Y, Lee JH, Zhu Y, Nazari M, Chen C, Wang H, Bernussi A, Holtz M, Fan Z. Structural, electrical, and terahertz transmission properties of VO_2 thin films grown on *c*-, *r*-, and *m*-plane sapphire substrates. J Appl Phys. 2012;111(5):053533. https://doi.org/10.1063/1.3692391
47. Cao L, Zhang X, Yuan J, Guo L, Hong T, Hang W, Ma Y. Study on the influence of sapphire crystal orientation on its chemical mechanical polishing. Appl Sci. 2020;10(22):8065. https://doi.org/10.3390/app10228065
48. Carter CB, Norton MG. Ceramic materials: science and engineering. New York: Springer; 2013. https://doi.org/10.1007/978-1-4614-3523-5_11
49. Goriki N, Miyake H, Hiramatsu K, Akiyama T, Ito T, Eryu O. AlN grown on *a*- and *n*-plane sapphire substrates by low-pressure hydride vapor phase epitaxy. Jpn J Appl Phys. 2013;52(8S):08JB31. https://doi.org/10.7567/JJAP.52.08JB31
50. Nakasu T, Aiba T, Yamashita S, Hattori S, Kizu T, Sun W-C, et al. Growth of ZnTe epilayers on *r*- and *n*-plane sapphire substrates. Jpn J Appl Phys. 2015;54(7):075501. https://doi.org/10.7567/JJAP.54.075501
51. Cryscore. Specified orientation sapphire wafers. c2022. Available from: https://www.cryscore.com/products/specified-orientation-sapphire-wafers.html
52. Yu Q, Qin G, Li H, Xia Z, Nian Y, Pei S-S. Mechanism of horizontally aligned growth of single-wall carbon nanotubes on R-plane sapphire. J Phys Chem B. 2006;110(45):22676–80. https://doi.org/10.1021/jp064875x
53. Nakamura T, Matsuhashi H, Nagatomo Y. Silicon on sapphire (SOS) device technology. Oki Techn Rev. 2004;71(4):66–69.
54. Stern AG, Cole DC. Design of a back-illuminated, crystallographically etched, silicon-on-sapphire avalanche photodiode with monolithically integrated microlens, for dual-mode passive & active imaging arrays. Proc. SPIE 7153, Lidar remote sensing for environmental monitoring IX, 71530Z. Noumea: New Caledonia; 2008. p. 135–47. https://doi.org/10.1117/12.804846
55. Munro RG. Evaluated material properties for a sintered α-alumina. J Am Ceram Soc. 1997;80(8):1919–28. https://doi.org/10.1111/j.1151-2916.1997.tb03074.x
56. Abyzov AM. Aluminum oxide and alumina ceramics (review). Part 1. Properties of Al_2O_3 and commercial production of dispersed Al_2O_3. Refract Industr Ceramics. 2019;60(1):24–32. https://doi.org/10.1007/s11148-019-00304-2
57. Riley FL. Structural ceramics—fundamentals and case studies. Cambridge: Cambridge University Press; 2009.
58. Barsoum MW. Fundamentals of ceramics, 2nd ed. Boca Raton: CRC Press; 2019. https://doi.org/10.1201/9781498708166
59. Liu Y, Liu Y, Drew MGB. Comparison of calculations for interplanar distances in a crystal lattice. Cryst Rev. 2017;23(4):252–301. https://doi.org/10.1080/0889311X.2017.1323332
60. Verma AR, Strivastava ON. Crystallography for solid state physics. New York: Wiley; 1982.
61. Nabarro FRN. Theoretical and experimental estimates of the Peierls stress. Phil Mag A. 1997;75(3):703–11.
62. Lubarda VA, Markenscoff X. Configurational force on a lattice dislocation and the Peierls stress. Arch Appl Mech. 2007;77(2–3):147–54. https://doi.org/10.1007/s00419-006-0068-y
63. Rodríguez MC, Castaing J, Munoz A, Veyssiere P, Rodríguez AD. Analysis of a kink pair model applied to a Peierls mechanism in basal and prism plane slips in sapphire (α-Al_2O_3) deformed between 200° and 1800°C. J Am Ceram Soc. 2008;91(5):1612–17. https://doi.org/10.1111/j.1551-2916.2008.02317.x
64. Kamimura Y, Edagawa K, Takeuchi S. Experimental evaluation of the Peierls stresses in a variety of crystals and their relation to the crystal structure. Acta Mater. 2013;61(1):294–309. https://doi.org/10.1016/j.actamat.2012.09.059
65. Lubarda VA. Dislocation Burgers vector and the Peach–Koehler force: a review. J Mater Res Tech. 2019;8(1):1550–65. https://doi.org/10.1016/j.jmrt.2018.08.014

How to cite this article: Lubarda VA, Lubarda MV. On the anion and cation positions within and nearby $R(10\bar{1}2)$, $\Sigma(20\bar{2}4)$, and $\Pi(10\bar{1}4)$ planes of α-Al_2O_3 corundum structure. J Am Ceram Soc. 2022;1–16. https://doi.org/10.1111/jace.18871